

RIScatter: Unifying Backscatter Communication and Reconfigurable Intelligent Surface From a Distribution Perspective

Yang Zhao, *Member, IEEE*, and Bruno Clerckx, *Fellow, IEEE*, TODO

Abstract—Backscatter Communication (BackCom) nodes harvest energy from and modulate information over an external electromagnetic wave. Reconfigurable Intelligent Surface (RIS) adapts its phase shift response to enhance or suppress equivalent channel strength in specific directions. In this paper, we show how both seemingly different technologies and their derivatives can be unified to leverage their benefits simultaneously into a single architecture called RIScatter. Envisioned as a next-generation communication protocol, RIScatter consists of multiple dispersed or co-located scatter nodes whose reflection states can be adapted to partially engineer the equivalent channel of the existing link and partially modulate their own information onto the scattered wave. This contrasts with BackCom (resp. RIS) where the reflection pattern is exclusively a function of the information symbol (resp. Channel State Information (CSI)). The key principle in RIScatter is to render the probability distribution of reflection states as a joint function of the information source, CSI, and Quality of Service (QoS) of both coexisting links. This enables RIScatter to softly bridge, generalize, and outperform BackCom and RIS; boil down to either under specific input distribution; or evolve in a mixed form for heterogeneous traffic control and universal hardware design. For a single-user multi-node RIScatter network, we characterize the achievable primary-(total)-backscatter rate region by optimizing the input distribution at the nodes, the active beamforming at the Access Point (AP), and the backscatter detection regions at the user. Simulation results demonstrate RIScatter nodes can exploit the additional propagation paths to smoothly transition between backscatter modulation and passive beamforming via smart input distribution design, and the proposed practical receiver effectively accommodates the double modulation and signal difference in active-passive coexisting networks.

I. INTRODUCTION

A. Fundamentals

FUTURE wireless network is envisioned to provide high throughput, uniform coverage, pervasive connectivity, heterogeneous control, and cognitive intelligence for trillions of portable devices. As a mature low-power communication technique, Backscatter Communication (BackCom) separates a conventional transmitter into a Radio-Frequency (RF) carrier emitter with power-hungry elements (e.g., synthesizer and amplifier) and an information-bearing node with power-efficient components (e.g., harvester and modulator) [1]. In particular, the node harvests energy from impinging wave and embeds information over scattered signal, while the backscatter reader can be either co-located or separated with the carrier emitter, known as Monostatic Backscatter Communication (MBC) and

Bistatic Backscatter Communication (BBC) in Fig. 1(a) and 1(b), respectively. Its applications such as Radio-Frequency Identification (RFID) [2], [3] and passive sensor network [4], [5] have been extensively researched, standardized, and commercialized in the era of Internet of Everything (IoE). However, conventional BackCom nodes only respond when externally inquired by a nearby reader. Ambient Backscatter Communication (AmBC) was then proposed in [6] where battery-free nodes recycle ambient signals (e.g., radio, television and Wi-Fi) to harvest energy and establish connection in between. As shown in Fig. 1(c), it eliminates the need of dedicated power supply, carrier emitter and frequency spectrum, but is subject to the strong direct-link interference. To tackle this, [7] proposed cooperative AmBC where both primary (legacy) and backscatter links are decoded by the same receiver under various detection schemes. The concept was further refined as Symbiotic Radio (SR) illustrated in Fig. 1(d) that cognitively incorporates AmBC with existing systems [8]. In a SR system, the active transmitter generates RF wave carrying primary information, the passive node provides extra propagation path and ride its information over scattered signal, while the cooperative receiver jointly or sequentially decodes both links. Those BackCom applications employ scatter nodes as pure information sources, and the primary link (if it exists) is indeed influenced by the randomness of backscatter modulation. On the other hand, Reconfigurable Intelligent Surface (RIS) is a smart planar signal reflector that consists of numerous compact passive elements with adjustable amplitude and phase responses. The reflection pattern is deterministic over time that can be adaptively optimized and coordinated in real time. RIS recycles and redistributes the surrounding RF waves to customize the wireless propagation environment for signal enhancement, interference suppression, scattering enrichment and non-line-of-sight bypassing [9].

B. Related Works

Similar to Cognitive Radio (CR), the coexistence of primary and backscatter links in SR can be classified into commensal, parasitic, and competitive relationships, whose instantaneous rates, power schemes, and outage probabilities were acquired in [10], [11]. Joint Maximum-Likelihood (ML) decoding provides the best error performance for SR but requires prohibitive computational complexity especially for high-order modulations [7]. One special property of those active-passive coexisting networks is that the backscatter signal strength can be relatively

The authors are with the Department of Electrical and Electronic Engineering, Imperial College London, London SW7 2AZ, U.K. (e-mail: {yang.zhao18, b.clerckx, TODO}@imperial.ac.uk).

TABLE I
COMPARISON OF SCATTERING APPLICATIONS

	MBC/BBC	AmBC	SR	RIS	RIScatter
Coexisting link(s)	1	2 (competitive)	2 (collaborative)	1	2 (collaborative)
Backscatter modulation	Yes	Yes	Yes	No	Yes
Scatterer impact on primary link	—	Interference	Channel uncertainty	Passive beamforming	Dynamic passive beamforming
Cooperative transmission(s)	—	No	Primary transmitter (active beamforming)	—	Primary transmitter and scatter nodes
Co-located receiver	—	No	Usually SIC from primary to backscatter	—	No SIC, backscatter detection as part of primary channel training
Primary detection	—	Semi-coherent	Semi-coherent	Coherent	Coherent
Backscatter detection	Coherent	Semi-coherent	Coherent	—	Semi-coherent
Reflection pattern depends on	Information source	Information source	Information source	CSI	Information source, CSI, and QoS
Input distribution	Equiprobable	Equiprobable	Equiprobable or Gaussian	Degenerate	Flexible
Load-switching speed	Fast	Fast or slow	Very slow	Quasi-static	Flexible

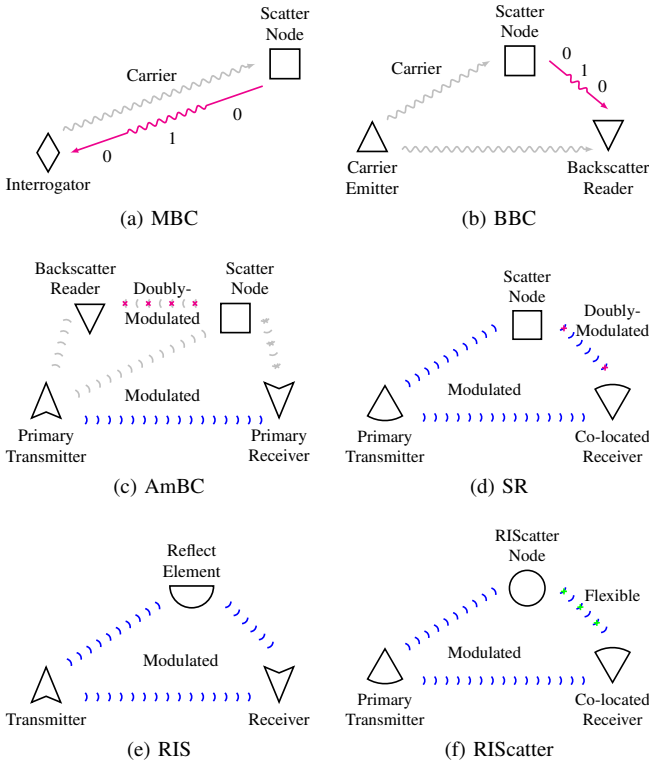


Fig. 1. Illustration of scattering applications. The blue paths constitute the primary link while the magenta/green paths denote the backscatter link.

weak due to the double fading effect. It motivated [7], [8], [10]–[18] to view SR as a multiplicative Non-Orthogonal Multiple Access (NOMA) and perform SIC from primary to backscatter link. During primary decoding, the backscatter randomness can be modelled as either interference or channel uncertainty, depending on the ratio N of primary sampling rate over backscat-

ter load-switching speed¹. Such a sequential SIC involves N re-encoding, precoding, subtraction together with a time-domain Maximal Ratio Combining (MRC) to decode each backscatter symbol, which can be operation-intensive and CSI-sensitive. When N is sufficiently large (i.e., commensal SR), the average primary achievable rate under noncoherent detection asymptotically approaches its coherent counterpart, and both links can be decoded in an interference-free manner [12]. A comparison of different scattering applications is summarized in Table I.

Another open issue for BackCom is the efficient backscatter multiple access design. [15] proposed a NOMA-based SR where the SIC order depends on the backscatter channel strength, but the performance deteriorates fast as the number of nodes increases. Time-Division Multiple Access (TDMA)-based SR was also considered in [16] where each node transmits information during its dedicated slot and harvests energy during others. It enables adaptive transmission time and reflection ratio optimization but incurs high coordination cost. [20] modifies the load-switching speed to shift the scattered signal to the desired frequency band. This enables backscatter Frequency-Division Multiple Access (FDMA) at the cost of extra bandwidth and higher node power consumption. To reduce coordination burden for passive nodes, [17] proposed a random code-assisted multiple access for SR and evaluated the asymptotic Signal-to-Interference-plus-Noise Ratio (SINR) using random matrix theory. However, this code-domain solution suffers from the near-far problem and imperfect synchronization, both can be very severe in practical scenarios.

Conventional RIS design with fixed reflection coefficients during each channel block has been extensively studied in communication, sensing, and power literatures [21]–[26]. On the other hand, dynamic RIS with independent reflection

¹For state-of-the-art low-power RFID tags, the load-switching speed usually varies between 100s of kHz to 10s of MHz [19], suggesting a typical N between 10 and 1000.

patterns at different transmission phases has gained recent attentions in multi-user and multi-purpose wireless networks. The concept was first proposed in [27] to fine-tune the Orthogonal Frequency-Division Multiplexing (OFDM) resource blocks, then extended to the downlink power and uplink information phases of Wireless Powered Communication Network (WPCN) [28]–[30]. It introduces artificial channel diversity and enables flexible resource allocation, but misses the opportunity to encode message at the RIS. When placed in the near field of a carrier emitter, RIS can also be used as a transmitter, and prototypes for Phase Shift Keying (PSK) and Quadrature Amplitude Modulation (QAM) have been implemented in [31], [32]. From an information-theoretic perspective, [33] reported that using RIS as a naive passive beamformer to maximize the Signal-to-Noise Ratio (SNR) is generally rate-suboptimal for finite input constellations. Instead, the capacity of RIS-aided channel is achieved by joint transmitter-RIS encoding, and multiplication coding with SIC decoding (i.e., SIC-based SR) can outperform passive beamforming at high SNR. It inspired RIS-empowered BackCom [34]–[43] to combine passive beamforming and backscatter modulation in the overall reflection pattern. In particular, *symbol level precoding* maps the information symbols to the optimized RIS coefficient sets [34], [35], *overlay modulation* superposes the information symbols over a common auxiliary matrix [36]–[39], *spatial modulation* switches between the reflection coefficient sets that maximize SNR at different receive antennas [40]–[42], and *index modulation* employs dedicated reflection elements (resp. information elements) for passive beamforming (resp. backscatter modulation) [43]. Those RIS-empowered BackCom designs can recycle RF wave on the air and employ scattered paths to boost wireless channels and establish new connections, but incurs advanced hardware architecture and high optimization complexity.

C. Contributions

First, we propose RIScatter as a novel scatter protocol that unifies BackCom and RIS from a distribution perspective. As shown in Fig. 1(f), the passive RIScatter node rides over an active transmission and controls the scattered wave to partially engineer the wireless channel and partially modulate its own information. This is accomplished by incorporating both the CSI and QoS into the reflection state distribution design. As such, RIScatter can generalize BackCom (uniform distribution) and RIS (degenerate distribution) to create a tradeoff between backscatter modulation and passive beamforming. This is the first paper to associate BackCom and RIS from a distribution perspective.

Second, we propose a practical receiver that accommodates the double modulation and signal difference in active-passive coexisting networks. Since the primary and backscatter messages are superimposed by multiplication coding and the backscatter symbol is typically longer than primary, the scattered signals from RIScatter nodes can be treated as multipath components during primary decoding, and the primary symbols can be viewed as a spreading code during backscatter decoding. Conventional sequential primary-backscatter decoder eliminates primary interference by SIC at each primary

block, while our sequential backscatter-primary detector semi-coherently decodes RIScatter nodes from the received energy, re-encodes to recover exact reflection patterns, and models the deterministic multipath within primary equivalent channel as dynamic passive beamforming at each backscatter block. It enables backscatter modulation and dynamic passive beamforming at much lower operational complexity, and is suitable for scatter nodes with various load-switching speeds.

Third, we consider a scenario where multiple RIScatter nodes ride over an active point-to-point Multiple-Input Single-Output (MISO) transmission to perform backscatter modulation and passive beamforming towards a nearby user using shared spectrum, energy, and infrastructures. We provide primary and total backscatter rate analyses and characterize the achievable rate region by optimizing input distribution at RIScatter nodes, active beamforming at the Access Point (AP), and backscatter decision regions at the user. Since the original problem is highly non-convex, we decouple it into individual subproblems and propose a suboptimal Block Coordinate Descent (BCD) algorithm, where the Karush-Kuhn-Tucker (KKT) input distribution is numerically evaluated by limit of sequences, the active beamforming is iteratively updated by Projected Gradient Descent (PGD) accelerated by Backtracking Line Search (BLS), and the decision regions are refined by existing sequential quantization methods for Discrete Memoryless Thresholding Channel (DMTC). This is the first paper to reveal the importance of input distribution and decision region designs in relevant literatures.

Fourth, we provide numerical results to demonstrate the benefits of RIScatter and proposed algorithms. We conclude: 1) adaptive reflection state distribution design can flexibly transition between backscatter modulation and passive beamforming; 2) when primary link is prioritized, input distribution becomes degenerate and RIScatter nodes coincide with discrete RIS; 3) when backscatter link is prioritized, adaptive RIScatter encoding achieves higher backscatter rate than conventional line coding with equiprobable inputs; 4) co-located RIScatter nodes can further leverage total backscatter rate by joint encoding; 5) the proposed receiver provides comparable backscatter detection performance than SIC-based SR while significantly reduces the encoding and precoding (and avoids subtraction) costs; 6) it also supports fast-switching nodes for higher backscatter throughput per unit time; 7) PGD active beamformer enlarges achievable rate region by boosting the receive SNR and/or widening the energy gap under different reflection states; 8) distribution-adaptive backscatter detectors provide higher total backscatter rate than the conventional ML detector.

Notations: Italic, bold lower-case, and bold upper-case letters denote scalars, vectors and matrices, respectively. $\mathbf{0}$ and $\mathbf{1}$ denote zero and one array of appropriate size, respectively. $\mathbb{I}^{x \times y}$, $\mathbb{R}_+^{x \times y}$, and $\mathbb{C}^{x \times y}$ denote the real unit, real nonnegative, and complex spaces of dimension $x \times y$, respectively. j denotes the imaginary unit. $\text{diag}(\cdot)$ returns a square matrix with the input vector on its main diagonal and zeros elsewhere. $\text{card}(\cdot)$ returns the cardinality of a set. $(\cdot)^*$, $(\cdot)^T$, $(\cdot)^H$, $|\cdot|$, and $\|\cdot\|$ denote the conjugate, transpose, conjugate transpose, absolute value, and Euclidean norm operators, respectively. $(\cdot)^{(r)}$ and $(\cdot)^*$ denote the r -th iterated and terminal solutions, respectively. The distribution of a Circularly Symmetric Complex Gaussian

(CSCG) random variable with zero mean and variance σ^2 is denoted by $\mathcal{CN}(0, \sigma^2)$, and \sim means “distributed as”.

II. SCATTERING PRINCIPLES

RF wave scattering and reflecting are usually realized by a *variable-load antenna* or *programmable metamaterial* and described by a unified signal model [44]. A typical antenna-based scatterer consists of an integrated antenna, a load-switching modulator, an energy harvester, and on-chip components (e.g., microcontroller and sensors) [2]. It first receives the impinging signals, then reradiates some back to the space and dissipates the remaining. In comparison, a typical metamaterial-based scatterer comprises an outer metamaterial layer of numerous sub-wavelength metallic/dielectric patches with tunable permittivity/permeability, a middle copper plate layer that reflects residual to avoid leakage, an inner circuit board layer that adjusts the amplitude and phase responses of patches, and an integrated microcontroller/FPGA that coordinates with the network and controls the circuit [45]. Ideally, it reflects the incident waves at the air-metamaterial boundary without receiving them, and mainly applies a phase shift on the reflected wave. In practice, both types of scatterers have finite reflection states with non-zero reflection loss, and the scattered signal can be decomposed into the *structural* and *antenna* mode components [46]. The former consistently contributes to environment multipath and can be modelled within CSI, while the latter depends on impedance mismatch and can be used for backscatter modulation and/or passive beamforming. For a scatter node with M reflection states, the reflection coefficient at state $m \in \mathcal{M} \triangleq \{1, \dots, M\}$ is

$$\Gamma_m = \frac{Z_m - Z^*}{Z_m + Z}, \quad (1)$$

where Z_m is the antenna load (resp. metamaterial unit) impedance at state m and Z is the antenna input (resp. medium characteristic) impedance. BackCom employ scatter nodes as information sources that encode message by *probabilistically switching* between different states. For M -ary QAM, constellation point c_m maps to reflection coefficient Γ_m by [47]

$$\Gamma_m = \alpha \frac{c_m}{\max_{m'} |c_{m'}|}, \quad (2)$$

where $\alpha \in \mathbb{I}$ is the amplitude scattering ratio at the direction of interest. In contrast, RIS employ reflect elements as channel reconfigurators that enable constructive/destructive signal superposition by *deterministically choosing* the reflection pattern. For a RIS element with M available states, phase shift θ_m maps to reflection coefficient Γ_m by [21]

$$\Gamma_m = \beta_m \exp(j\theta_m), \quad (3)$$

where $\beta_m \in \mathbb{I}$ is the overall amplitude scattering ratio of state m .²

III. RISCATTER

A. Concepts

As a generalization of BackCom and RIS, RIScatter is a passive scatter protocol that coexists with an active primary

system in a flexible and mutualistic manner. RIScatter nodes leverage CSI- and QoS-based input distribution design to smoothly transition between backscatter modulation and passive beamforming. It can be implemented by adding an integrated receiver [48] and adaptive encoder [49] to off-the-shelf passive backscatter tags. The block diagram, equivalent circuit, and scatter model of a RIScatter node are illustrated in Fig. 2, while the input distribution and time structure comparison of scattering applications are shown in Fig. 3. Instead of using fully random or fully deterministic reflection pattern over time, each RIScatter node semi-randomly chooses the reflection state for each backscatter block with guidance of input probability distribution $P(\Gamma_m)$ at state m . Such an adaptive backscatter coding boils down to degenerate distribution of RIS when primary link is prioritized, and outperforms conventional line coding with equiprobable inputs (e.g., FM0 for RFID) when backscatter link is prioritized. Besides, joint encoding over multiple co-located RIScatter nodes can further boost the total backscatter rate. Relevant CSI can be acquired by existing low-power estimation techniques. For dispersed RIScatter nodes, the cascaded transmitter-node-receiver channels can be estimated by sequential [51]–[53] or parallel approaches [54] originally proposed for BackCom. For co-located RIScatter nodes, the estimation can be simplified by group-based [55] and hierarchical [56] trainings originally proposed for RIS.

Remark 1. *Scatter-based multiple access involves a double modulation where the primary and backscatter symbols of different length are superimposed by multiplication coding. The reflection pattern not only encodes the backscatter message, but also affects the primary equivalent channel. Therefore, backscatter detection under primary uncertainty can be viewed as part of primary channel training, and novel decoding strategies apart from SIC³ is desired for RIScatter.*

Next, we propose a cooperative receiver that effectively exploit signal characteristics (i.e., double modulation and symbol period difference) to reduce the decoding complexity and improve the primary-backscatter tradeoff. As illustrated in Fig. 4, conditioned on different reflection state hypotheses, the accumulated receive energy per backscatter block follows Gamma distribution with different scale parameters [57]. Hence, the receiver can semi-coherently (in the presence of primary uncertainty) decode node messages from the accumulated receive energy, re-encode to recover actual reflection patterns, and model the deterministic multipath within primary equivalent channel. It enables simultaneous backscatter modulation and dynamic passive beamforming by only one energy comparison, re-encoding, and precoding operations for each backscatter block (instead of primary block), and is suitable for arbitrary primary sampling rate and backscatter load-switching speed.

²Most existing RIS literatures assume lossless reflection $\beta_m = 1, \forall m$.

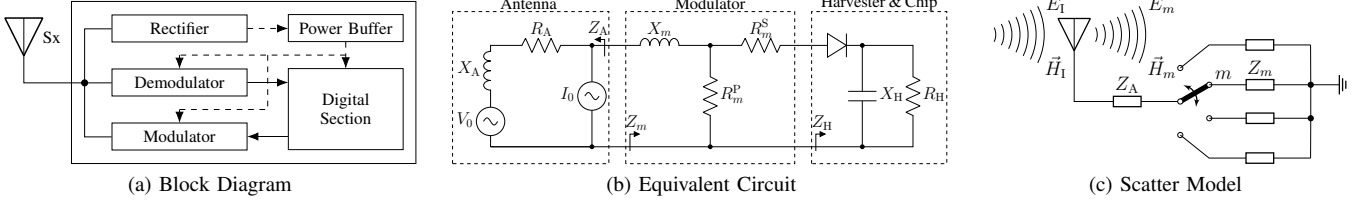


Fig. 2. Block diagram, equivalent circuit, and scatter model of a RIScatter node. The solid and dashed vectors represent signal and energy flows. The scatter antenna behaves as a constant power source, where the voltage V_0 and current I_0 are introduced by incident electric field \vec{E}_I and magnetic field \vec{H}_I [50].

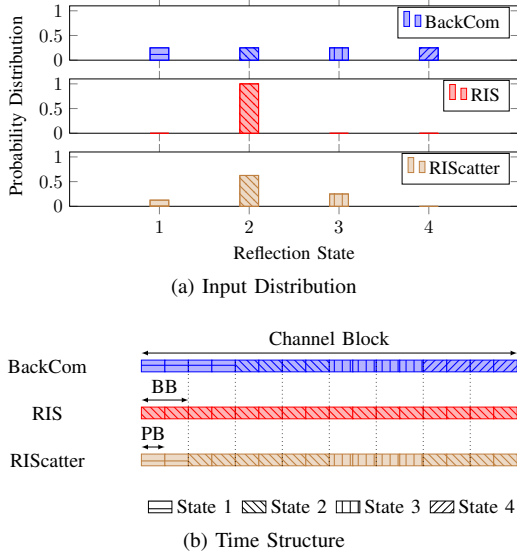


Fig. 3. Input distribution and time structure of BackCom, RIS, and RIScatter. “PB” means primary block and “BB” means backscatter block.

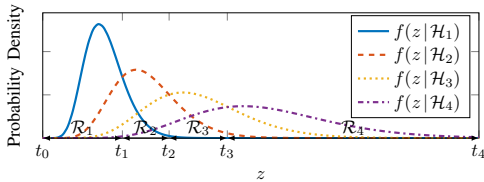


Fig. 4. PDF of accumulated receive energy per backscatter block conditioned on different reflection state hypotheses. z , t , \mathcal{H} and \mathcal{R} denote the accumulated receive energy, decision threshold, reflection state hypothesis, and decision regions, respectively.

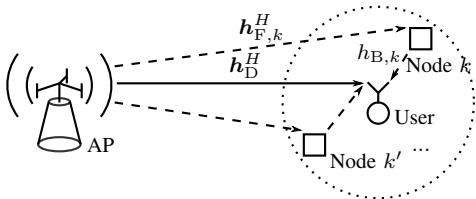


Fig. 5. A single-user multi-node RIScatter system.

B. System Model

As shown in Fig. 5, we consider an active-passive coexisting network where a Q -antenna AP serves a single-antenna user and K nearby dispersed and/or co-located single-antenna RIScatter nodes each with M available states. In the primary point-to-point system, the AP transmits information to the user over the multipath channel enhanced by RIScatter nodes. In the backscatter MAC system, the AP and user become carrier emitter and backscatter reader, and the RIScatter nodes modulate over scattered RF signals. For simplicity, we consider a quasi-static block fading model where channels remain constant within each block and vary independently between consecutive blocks, and assume the backscatter-over-primary symbol period ratio N is an integer. We also omit the signal reflected by two or more times and ignore the propagation time difference of different paths. Denote the AP-user direct channel as $\mathbf{h}_D^H \in \mathbb{C}^{1 \times Q}$, the AP-node $k \in \mathcal{K} \triangleq \{1, \dots, K\}$ forward channel as $\mathbf{h}_{F,k}^H \in \mathbb{C}^{1 \times Q}$, the node k -user backward channel as $h_{B,k}$, and the cascaded AP-node k -user channel as $\mathbf{h}_{C,k}^H \triangleq h_{B,k} \mathbf{h}_{F,k}^H \in \mathbb{C}^{1 \times Q}$. Let $x_k \in \mathcal{X} \triangleq \{c_1, \dots, c_M\}$ be the coded backscatter symbol of node k and $\mathbf{x}_K \triangleq (x_1, \dots, x_K)$ be the backscatter symbol tuple of all nodes. Without loss of generality, we consider one backscatter block (i.e., N primary blocks) in the following context. Due to double modulation, the primary equivalent channel is a function of backscatter symbol tuple⁴

$$\mathbf{h}_E^H(\mathbf{x}_K) \triangleq \mathbf{h}_D^H + \sum_k \alpha_k \mathbf{h}_{C,k}^H x_k \quad (4a)$$

$$= \mathbf{h}_D^H + \mathbf{x}^H \text{diag}(\boldsymbol{\alpha}) \mathbf{H}_C, \quad (4b)$$

where $\alpha_k \in \mathbb{I}$ is the amplitude scattering ratio of node k , $\boldsymbol{\alpha} \triangleq [\alpha_1, \dots, \alpha_K]^T \in \mathbb{I}^K$, $\mathbf{x} \triangleq [x_1, \dots, x_K]^H \in \mathcal{X}^K$, and $\mathbf{H}_C \triangleq [\mathbf{h}_{C,1}, \dots, \mathbf{h}_{C,K}]^H \in \mathbb{C}^{K \times Q}$. The signal received by the user at primary block $n \in \mathcal{N} \triangleq \{1, \dots, N\}$ is

$$y[n] = \mathbf{h}_E^H(\mathbf{x}_K) \mathbf{w} s[n] + v[n], \quad (5)$$

where $\mathbf{w} \in \mathbb{C}^Q$ is the active beamformer satisfying average transmit power constraint $\|\mathbf{w}\|^2 \leq P$, $s \sim \mathcal{CN}(0, 1)$ is the primary symbol, and $v \sim \mathcal{CN}(0, \sigma_v^2)$ is the Additive White Gaussian Noise (AWGN) with average power σ_v^2 . Let $m_k \in \mathcal{M} \triangleq \{1, \dots, M\}$ be the reflection state index of node

³Superposition coding and SIC was originally proposed to achieve the capacity vertices of Gaussian Multiple Access Channel (MAC). For active-passive coexisting networks, SIC not only fails to utilize the multiplication coding/double modulation, but also requires N re-encoding, precoding and subtraction with a time-domain MRC during each backscatter block.

⁴(4a) and (4b) are often used in BackCom and RIS literatures, respectively.

k , $m_K \triangleq (m_1, \dots, m_K)$ be the state index tuple of all nodes, x_{m_k} be the backscatter symbol of node k indexed by m_k , and x_{m_K} be the backscatter symbol tuple indexed by m_K .⁵ Conditioned on m_K , the receive signal at each primary block follows CSCG distribution $\mathcal{CN}(0, \sigma_{m_K}^2)$, where

$$\sigma_{m_K}^2 = |\mathbf{h}_E^H(x_{m_K})\mathbf{w}|^2 + \sigma_v^2 \quad (6)$$

is the received variance. Let $z = \sum_n |y[n]|^2$ be the accumulated receive energy per backscatter block. Since z is the sum of N independent and identically distributed (i.i.d.) exponential variables, its conditional PDF follows Gamma distribution

$$f(z|\mathcal{H}_{m_K}) = \frac{z^{N-1} \exp(-z/\sigma_{m_K}^2)}{\sigma_{m_K}^{2N} (N-1)!}, \quad (7)$$

where \mathcal{H}_{m_K} denotes hypothesis m_K . At the receiver, the energy space is divided into disjoint decision regions associated with different hypotheses, as illustrated in Fig. 4.

Remark 2. *The capacity-achieving decision region design for DMTC with non-binary inputs in arbitrary distribution remains an open issue. It was proved deterministic detector can be rate-optimal, but non-convex decision regions (i.e., comprise non-adjacent partitions) are generally required and the optimal number of thresholds is still unknown [58], [59]. Hence, we limit the backscatter energy detector to convex deterministic decision regions and consider sequential threshold design in the following context.*

For the ease of notations, we map the state index tuple m_K to the corresponding index $l \in \mathcal{L} \triangleq \{1, \dots, L \triangleq M^K\}$, where $\sigma_1^2, \dots, \sigma_L^2$ is an ascending sequence. Both notations are used interchangeably in the following context. As such, the decision region of backscatter symbol tuple l can be written as

$$\mathcal{R}_l \triangleq [t_{l-1}, t_l], \quad 0 \leq t_{l-1} \leq t_l, \quad (8)$$

where t_l is the energy decision threshold between hypotheses \mathcal{H}_l and \mathcal{H}_{l+1} . For a given decision threshold vector $\mathbf{t} \triangleq [t_0, \dots, t_L]^T \in \mathbb{R}_+^{(L+1)}$, we can formulate a Discrete Memoryless Thresholding Multiple Access Channel (DMTMAC) with transition probability from input x_{m_K} to output $\hat{x}_{m'_K}$ given by

$$P(\hat{x}_{m'_K}|x_{m_K}) = \int_{\mathcal{R}_{m'_K}} f(z|\mathcal{H}_{m_K}) dz, \quad (9)$$

over which adaptive input distribution design and backscatter channel coding can be performed.

C. Achievable Rates

Let $P_k(x_{m_k})$ be the input probability of node k at state m_k , and $\mathbf{p}_k \triangleq [P_k(c_1), \dots, P_k(c_M)]^T \in \mathbb{I}^M$ be the input distribution vector. For dispersed nodes with independent encoding, the probability of backscatter symbol tuple x_{m_K} is

$$P_K(x_{m_K}) = \prod_{k \in \mathcal{K}} P_k(x_{m_k}). \quad (10)$$

⁵Please note x_k and x_K are discrete random variable and tuple, while x_{m_k} and x_{m_K} are their values indexed by m_k and m_K .

Following [60], we define the backscatter information function between input symbol tuple instance x_{m_K} and output symbol tuple variable \hat{x}_K as

$$I_B(x_{m_K}; \hat{x}_K) \triangleq \sum_{m'_K} P(\hat{x}_{m'_K}|x_{m_K}) \log \frac{P(\hat{x}_{m'_K}|x_{m_K})}{P_K(\hat{x}_{m'_K})}, \quad (11)$$

where $P_K(\hat{x}_{m'_K}) = \sum_{m_K} P_K(x_{m_K}) P(\hat{x}_{m'_K}|x_{m_K})$ is the probability of output tuple $\hat{x}_{m'_K}$. We also define the backscatter marginal information of letter x_{m_k} as

$$I_{B,k}(x_{m_k}; \hat{x}_K) \triangleq \sum_{m_{K \setminus \{k\}}} P_{K \setminus \{k\}}(x_{m_{K \setminus \{k\}}}) I_B(x_{m_K}; \hat{x}_K), \quad (12)$$

where $P_{K \setminus \{k\}}(x_{m_{K \setminus \{k\}}}) = \prod_{q \in \mathcal{K} \setminus \{k\}} P_q(x_{m_q})$. Hence, the backscatter mutual information can be written as

$$I_B(x_K; \hat{x}_K) = \sum_{m_K} P_K(x_{m_K}) I_B(x_{m_K}; \hat{x}_K). \quad (13)$$

Once node messages are successfully decoded, we can re-encode for exact backscatter symbol tuple x_K , recover their reflection patterns by (2), and retrieve the primary equivalent channel by (4). Therefore, the primary information function conditioned on backscatter symbol tuple x_{m_K} is

$$I_P(s; y|x_{m_K}) \triangleq \log \left(1 + \frac{|\mathbf{h}_E^H(x_{m_K})\mathbf{w}|^2}{\sigma_v^2} \right), \quad (14)$$

the primary marginal information of letter x_{m_k} is

$$I_{P,k}(s; y|x_{m_k}) \triangleq \sum_{m_{K \setminus \{k\}}} P_{K \setminus \{k\}}(x_{m_{K \setminus \{k\}}}) I_P(s; y|x_{m_K}), \quad (15)$$

and the average primary mutual information is

$$I_P(s; y|x_K) = \sum_{m_K} P_K(x_{m_K}) I_P(s; y|x_{m_K}). \quad (16)$$

With a slight abuse of notation, we define the corresponding weighted sum information function, marginal information, and mutual information as

$$I(x_{m_K}) \triangleq \rho I_P(s; y|x_{m_K}) + (1-\rho) I_B(x_{m_K}; \hat{x}_K), \quad (17)$$

$$I_k(x_{m_k}) \triangleq \rho I_{P,k}(s; y|x_{m_k}) + (1-\rho) I_{B,k}(x_{m_k}; \hat{x}_K), \quad (18)$$

$$I(x_K) \triangleq \rho I_P(s; y|x_K) + (1-\rho) I_B(x_K; \hat{x}_K), \quad (19)$$

where $\rho \in \mathbb{I}$ is the QoS of the primary link. We notice the average primary rate (16) depends on the input distribution and active beamforming, while the total backscatter rate depends on the input distribution and DMTMAC (9) that relates to active beamforming and decision thresholds.

IV. RATE-REGION CHARACTERIZATION

To characterize the achievable primary-(total)-backscatter rate region for the RIScatter system in Fig. 5, we aim to maximize the weighted sum rate with respect to input distribution $\{\mathbf{p}_k\}_{k \in \mathcal{K}}$, active beamforming \mathbf{w} , and decision thresholds \mathbf{t} by

$$\max_{\{\mathbf{p}_k\}_{k \in \mathcal{K}}, \mathbf{w}, \mathbf{t}} I(x_K) \quad (20a)$$

$$\text{s.t.} \quad \mathbf{1}^T \mathbf{p}_k = 1, \quad \forall k, \quad (20b)$$

$$\mathbf{p}_k \geq \mathbf{0}, \quad \forall k, \quad (20c)$$

$$\|\mathbf{w}\|^2 \leq P, \quad (20d)$$

$$t_{l-1} \leq t_l, \quad \forall l, \quad (20e)$$

$$\mathbf{t} \geq \mathbf{0}. \quad (20f)$$

Problem (20) generalizes conventional BackCom by allowing CSI- and QoS-adaptive input distribution and detection region design. It also generalizes the discrete RIS phase shift selection by allowing stochastic reflection (i.e., relaxing the feasible domain from the vertices of M -dimensional probability simplex to the simplex itself). Since problem (20) is highly non-convex, we propose a BCD algorithm that iteratively updates $\{p_k\}_{k \in \mathcal{K}}$, \mathbf{w} and \mathbf{t} until convergence.

A. Input Distribution

For any given \mathbf{w} and \mathbf{t} , we can construct the equivalent DMTMAC by (9) and simplify (20) to

$$\max_{\{p_k\}_{k \in \mathcal{K}}} I(x_{\mathcal{K}}) \quad (21a)$$

$$\text{s.t.} \quad (20b), (20c), \quad (21b)$$

which is convex when $K=1$ or joint encoding⁶ over $K > 1$ co-located nodes is available. When the nodes are dispersed, problem (21) involves coupled term $\prod_{k \in \mathcal{K}} P_k(x_{m_k})$ and is non-convex. Following [60], we first recast the KKT conditions to their equivalent forms, then propose a numerical method that guarantees those conditions by limit of sequences.

Remark 3. As demonstrated in [61], KKT conditions are generally necessary but insufficient for total rate maximization of discrete MAC. We will show in the simulation part that, for a moderate K , the average achievable rate regions of KKT and global-optimal input distributions almost overlap with each other.

Proposition 1. The KKT optimality conditions for problem (21) are equivalent to, $\forall k, m_k$,

$$I_k^*(x_{m_k}) = I^*(x_{\mathcal{K}}), \quad P_k^*(x_{m_k}) > 0, \quad (22a)$$

$$I_k^*(x_{m_k}) \leq I^*(x_{\mathcal{K}}), \quad P_k^*(x_{m_k}) = 0. \quad (22b)$$

Proof. Please refer to Appendix A. \square

For each node, (22a) suggests each probable state should produce the same marginal information (averaged over all states of other nodes), while (22b) suggests any state with potentially less marginal information should not be used.

Proposition 2. For any strictly positive initializer $\{p_k^{(0)}\}_{k \in \mathcal{K}}$, the KKT input probability of node k at state m_k is given by the converging point of the sequence

$$P_k^{(r+1)}(x_{m_k}) = \frac{P_k^{(r)}(x_{m_k}) \exp\left(\frac{\rho}{1-\rho} I_k^{(r)}(x_{m_k})\right)}{\sum_{m'_k} P_k^{(r)}(x_{m'_k}) \exp\left(\frac{\rho}{1-\rho} I_k^{(r)}(x_{m'_k})\right)}, \quad (23)$$

where r is the iteration index.

Proof. Please refer to Appendix B. \square

For (23) at iteration $r+1$, the input distribution of node k is updated over $\{\{p_q^{(r+1)}\}_{q=1}^{k-1}, \{p_q^{(r)}\}_{q=k}^K\}$. The KKT input distribution design is summarized in Algorithm 1.

⁶Joint encoding formulates an equivalent source of M^K valid codewords, such that one can directly design $P_{\mathcal{K}}(x_{m_{\mathcal{K}}})$ instead of $P_k(x_{m_k})$.

Algorithm 1: Numerical KKT Input Distribution Evaluation by Limits of Sequence

Input: $K, N, \mathbf{h}_D^H, \mathbf{H}_C, \boldsymbol{\alpha}, \mathcal{X}, \sigma_v^2, \rho, \mathbf{w}, \mathbf{t}, \varepsilon$

Output: $\{p_k^*\}_{k \in \mathcal{K}}$

- 1: Set $\mathbf{h}_E^H(x_{m_{\mathcal{K}}}), \forall m_{\mathcal{K}}$ by (4)
- 2: $\sigma_{m_{\mathcal{K}}}^2, \forall m_{\mathcal{K}}$ by (6)
- 3: $f(z|\mathcal{H}_{m_{\mathcal{K}}}), \forall m_{\mathcal{K}}$ by (7)
- 4: $P(\hat{x}_{m'_k}|x_{m_{\mathcal{K}}}), \forall m_{\mathcal{K}}, m'_k$ by (9)
- 5: Initialize $r \leftarrow 0$
- 6: $\mathbf{p}_k^{(0)} > \mathbf{0}, \forall k$
- 7: Get $P_k^{(r)}(x_{m_{\mathcal{K}}}), \forall m_{\mathcal{K}}$ by (10)
- 8: $I_k^{(r)}(x_{m_{\mathcal{K}}}), \forall m_{\mathcal{K}}$ by (11), (14), (17)
- 9: $I_k^{(r)}(x_{m_k}), \forall k, m_k$ by (12), (15), (18)
- 10: $I^{(r)}(x_{\mathcal{K}})$ by (13), (16), (19)
- 11: **Repeat**
- 12: Update $r \leftarrow r+1$
- 13: $\mathbf{p}_k^{(r)}, \forall k$ by (23)
- 14: Redo step 7–10
- 15: **Until** $I^{(r)}(x_{\mathcal{K}}) - I^{(r-1)}(x_{\mathcal{K}}) \leq \varepsilon$

B. Active Beamforming

For any given $\{p_k\}_{k \in \mathcal{K}}$ and \mathbf{t} , problem (20) reduces to

$$\max_{\mathbf{w}} I(x_{\mathcal{K}}) \quad (24a)$$

$$\text{s.t.} \quad (20d), \quad (24b)$$

which is still non-convex due to the integration and entropy terms. To tackle this, we rewrite the DMTMAC transition probability (9) from input index tuple $m_{\mathcal{K}}$ to output index l as a regularized incomplete Gamma function in the series representation [62, Theorem 3]

$$\begin{aligned} Q\left(N, \frac{t_{l-1}}{\sigma_{m_{\mathcal{K}}}^2}, \frac{t_l}{\sigma_{m_{\mathcal{K}}}^2}\right) &= \frac{\int_{t_{l-1}/\sigma_{m_{\mathcal{K}}}^2}^{t_l/\sigma_{m_{\mathcal{K}}}^2} z^{N-1} \exp(-z) dz}{(N-1)!} \\ &= \exp\left(-\frac{t_{l-1}}{\sigma_{m_{\mathcal{K}}}^2}\right) \sum_{n=0}^{N-1} \frac{\left(\frac{t_{l-1}}{\sigma_{m_{\mathcal{K}}}^2}\right)^n}{n!} - \exp\left(-\frac{t_l}{\sigma_{m_{\mathcal{K}}}^2}\right) \sum_{n=0}^{N-1} \frac{\left(\frac{t_l}{\sigma_{m_{\mathcal{K}}}^2}\right)^n}{n!}. \end{aligned} \quad (25)$$

Its gradient with respect to \mathbf{w}^* can be derived as

$$\nabla_{\mathbf{w}^*} Q\left(N, \frac{t_{l-1}}{\sigma_{m_{\mathcal{K}}}^2}, \frac{t_l}{\sigma_{m_{\mathcal{K}}}^2}\right) = \frac{\mathbf{h}_E(x_{m_{\mathcal{K}}}) \mathbf{h}_E^H(x_{m_{\mathcal{K}}}) \mathbf{w}}{(\sigma_{m_{\mathcal{K}}}^2)^2} g_{m_{\mathcal{K}}}(t_{l-1}, t_l), \quad (26)$$

where $g_{m_{\mathcal{K}}}(t_{l-1}, t_l) \triangleq g_{m_{\mathcal{K}}}(t_l) - g_{m_{\mathcal{K}}}(t_{l-1})$ and

$$g_{m_{\mathcal{K}}}(t_l) = t_l \exp\left(-\frac{t_l}{\sigma_{m_{\mathcal{K}}}^2}\right) \left(-1 + \sum_{n=1}^{N-1} \frac{\left(n - \frac{t_l}{\sigma_{m_{\mathcal{K}}}^2}\right) \left(\frac{t_l}{\sigma_{m_{\mathcal{K}}}^2}\right)^{n-1}}{n!}\right). \quad (27)$$

On top of (25) and (26), we explicitly express the objective function (24a) and its gradient as (28) and (29) at the end of page 8, respectively. They allows problem (24) to be solved by the PGD method, where any unregulated beamformer $\bar{\mathbf{w}}$ can be projected onto the feasible domain of average transmit power constraint (20d) by

$$\mathbf{w} = \sqrt{P} \frac{\bar{\mathbf{w}}}{\max(\sqrt{P}, \|\bar{\mathbf{w}}\|)}. \quad (30)$$

Algorithm 2: Iterative Active Beamforming Optimization by PGD with BLS

Input: $Q, N, \mathbf{h}_D^H, \mathbf{H}_C, \alpha, \mathcal{X}, P, \sigma_v^2, \rho, \{\mathbf{p}_k\}_{k \in \mathcal{K}}, \mathbf{t}, \alpha, \beta, \gamma, \varepsilon$
Output: \mathbf{w}^*

```

1: Set  $\mathbf{h}_E^H(x_{m_K}), \forall m_K$  by (4)
2:  $P_K(x_{m_K}), \forall m_K$  by (10)
3: Initialize  $r \leftarrow 0$ 
4:  $\mathbf{w}^{(0)}, \|\mathbf{w}^{(0)}\|^2 \leq P$ 
5: Get  $(\sigma_{m_K}^{(r)})^2, \forall m_K$  by (6)
6:  $Q^{(r)}(N, \frac{t_{l-1}}{\sigma_{m_K}^2}, \frac{t_l}{\sigma_{m_K}^2}), \forall m_K, l$  by (25)
7:  $I^{(r)}(x_K)$  by (28)
8:  $\nabla_{\mathbf{w}^*} Q^{(r)}(N, \frac{t_{l-1}}{\sigma_{m_K}^2}, \frac{t_l}{\sigma_{m_K}^2}), \forall m_K, l$  by (26)
9:  $\nabla_{\mathbf{w}^*} I^{(r)}(x_K)$  by (29)
10: Repeat
11:   Update  $r \leftarrow r + 1$ 
12:    $\gamma^{(r)} \leftarrow \gamma$ 
13:    $\mathbf{w}^{(r)} \leftarrow \mathbf{w}^{(r-1)} + \gamma \nabla_{\mathbf{w}^*} I^{(r-1)}(x_K)$ 
14:    $\mathbf{w}^{(r)}$  by (30)
15:   Redo step 5–7
16:   While  $I^{(r)}(x_K) < I^{(r-1)}(x_K) + \alpha \gamma \|\nabla_{\mathbf{w}^*} I^{(r-1)}(x_K)\|^2$ 
17:     Set  $\gamma^{(r)} \leftarrow \beta \gamma^{(r)}$ 
18:     Redo step 13–15
19:   End While
20:   Redo step 8, 9
21: Until  $\|\mathbf{w}^{(r)} - \mathbf{w}^{(r-1)}\| \leq \varepsilon$ 

```

The PGD active beamforming optimization with adaptive BLS step size [63, Section 9.2] is summarized in Algorithm 2.

C. Decision Threshold

For any given $\{\mathbf{p}_k\}_{k \in \mathcal{K}}$ and \mathbf{w} , problem (20) reduces to

$$\max_{\mathbf{t}} I(x_K) \quad (31a)$$

$$\text{s.t.} \quad (20e), (20f), \quad (31b)$$

which is still non-convex because variable \mathbf{t} appears on the limits of integration (9). Fortunately, we can further simplify problem (31) as a point-to-point rate-optimal quantizer design for a discrete-input continuous-output memoryless channel, thanks to Remark 4 and 5.

Remark 4. Upon successful backscatter decoding, the user can always re-encode node messages to recover the exact reflection patterns and determine the primary equivalent channel at each backscatter block. Thus, backscatter decision design has no impact on the primary achievable rate, and any thresholding that maximize the total backscatter rate (13) is also optimal for problem (31).

Remark 5. In terms of total backscatter rate, the potentially dispersed nodes with known input distribution can be viewed as an equivalent source with backscatter symbol tuples as codewords. As such, the DMTMAC (9) becomes a DMTC and problem (31) reduces to the rate-optimal quantization design for a discrete-input continuous-output memoryless channel.

Next, we constrain the feasible domain of problem (31) from continuous space \mathbb{R}_+^{L+1} to finite candidate set (i.e., fine-grained discrete energy levels) \mathcal{T}^{L+1} . As shown in Fig. 6, by introducing the extra analog-to-digital conversion, we can group adjacent high-resolution energy bins to construct backscatter decision regions. Thus, problem (31) can be recast as

$$\max_{\mathbf{t} \in \mathcal{T}^{L+1}} I_B(x_K; \hat{x}_K) \quad (32a)$$

$$\text{s.t.} \quad (20e), \quad (32b)$$

which can be solved by existing rate-optimal sequential quantizer designs for DMTC. To obtain global optimal solution, [64] started from the quadrangle inequality and proposed a Dynamic Programming (DP) method accelerated by the Shor-Moran-Aggarwal-Wilber-Klawe (SMAWK) algorithm with computational complexity $\mathcal{O}(L^2(\text{card}(\mathcal{T}) - L))$, while [65] started from the optimality condition for three neighbor thresholds and presented a traverse-then-bisect algorithm with complexity $\mathcal{O}(\text{card}(\mathcal{T})L \log(\text{card}(\mathcal{T})L))$. In Section V, both schemes will be compared with the ML scheme [66]

$$t_l^{\text{ML}} = N \frac{\sigma_{l-1}^2 \sigma_l^2}{\sigma_{l-1}^2 - \sigma_l^2} \log \frac{\sigma_{l-1}^2}{\sigma_l^2}, \quad l \in \mathcal{L} \setminus \{L\}, \quad (33)$$

which is generally suboptimal for problem (31) except when all nodes are with equiprobable inputs.

V. SIMULATION RESULTS

In this section, we provide numerical results to evaluate the proposed input distribution, active beamforming, and

$$I(x_K) = \sum_{m_K} P_K(x_{m_K}) \left(\rho \log \left(1 + \frac{|\mathbf{h}_E^H(x_{m_K}) \mathbf{w}|^2}{\sigma_v^2} \right) + (1 - \rho) \sum_l Q \left(N, \frac{t_{l-1}}{\sigma_{m_K}^2}, \frac{t_l}{\sigma_{m_K}^2} \right) \log \frac{Q \left(N, \frac{t_{l-1}}{\sigma_{m_K}^2}, \frac{t_l}{\sigma_{m_K}^2} \right)}{\sum_{m'_K} P_K(x_{m'_K}) Q \left(N, \frac{t_{l-1}}{\sigma_{m'_K}^2}, \frac{t_l}{\sigma_{m'_K}^2} \right)} \right) \quad (28)$$

$$\begin{aligned} \nabla_{\mathbf{w}^*} I(x_K) = & \sum_{m_K} P_K(x_{m_K}) \left(\rho \frac{\mathbf{h}_E(x_{m_K}) \mathbf{h}_E^H(x_{m_K}) \mathbf{w}}{\sigma_{m_K}^2} + (1 - \rho) \sum_l \left(\log \frac{Q \left(N, \frac{t_{l-1}}{\sigma_{m_K}^2}, \frac{t_l}{\sigma_{m_K}^2} \right)}{\sum_{m'_K} P_K(x_{m'_K}) Q \left(N, \frac{t_{l-1}}{\sigma_{m'_K}^2}, \frac{t_l}{\sigma_{m'_K}^2} \right)} + 1 \right) \right. \\ & \times \nabla_{\mathbf{w}^*} Q \left(N, \frac{t_{l-1}}{\sigma_{m_K}^2}, \frac{t_l}{\sigma_{m_K}^2} \right) - \frac{Q \left(N, \frac{t_{l-1}}{\sigma_{m_K}^2}, \frac{t_l}{\sigma_{m_K}^2} \right) \sum_{m'_K} P_K(x_{m'_K}) \nabla_{\mathbf{w}^*} Q \left(N, \frac{t_{l-1}}{\sigma_{m'_K}^2}, \frac{t_l}{\sigma_{m'_K}^2} \right)}{\sum_{m'_K} P_K(x_{m'_K}) Q \left(N, \frac{t_{l-1}}{\sigma_{m'_K}^2}, \frac{t_l}{\sigma_{m'_K}^2} \right)} \Bigg) \end{aligned} \quad (29)$$

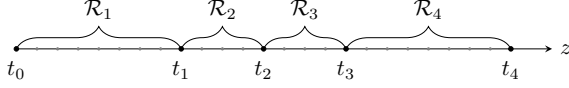


Fig. 6. The decision thresholds are selected from fine-grained discrete energy levels instead of continuous space, and each decision region consists of at least one neighbor energy bins.

backscatter decision designs for the RIScatter system in Fig. 5. We assume the AP-user distance is 10 m and at least one RIScatter nodes are randomly dropped in a disk centered at the user with radius r . The AP is with an average transmit power budget $P = 36\text{dBm}$ and all nodes employs M -QAM with amplitude scattering ratio $\alpha = 0.5$. For all channels involved, we consider a distance-dependent path loss model

$$L(d) = L_0 \left(\frac{d_0}{d} \right)^\gamma, \quad (34)$$

together with a Rician fading model

$$\mathbf{H} = \sqrt{\frac{\kappa}{1+\kappa}} \bar{\mathbf{H}} + \sqrt{\frac{1}{1+\kappa}} \tilde{\mathbf{H}}, \quad (35)$$

where d is the transmission distance, $L_0 = -30\text{dB}$ is the reference path loss at $d_0 = 1\text{m}$, κ is the Rician K -factor, $\bar{\mathbf{H}}$ is the deterministic line-of-sight component with unit-magnitude entries, and $\tilde{\mathbf{H}}$ is the Rayleigh fading component with standard i.i.d. CSCG entries. We choose $\gamma_D = 2.6$, $\gamma_F = 2.4$, $\gamma_B = 2$, and $\kappa_D = \kappa_F = \kappa_B = 5$ for direct, forward and backward links. The finite decision threshold domain \mathcal{T} is obtained by b -bit uniform discretization over the critical interval defined by the confidence bounds of edge hypotheses (i.e., lower bound of \mathcal{H}_1 and upper bound of \mathcal{H}_L) with confidence $1 - \varepsilon$, and we choose $b = 9$ and $\varepsilon = 10^{-3}$. All achievable rate points/regions are averaged over 1000 channel realizations.

A. Evaluation of Proposed Algorithms

1) *Initialization*: To characterize each achievable rate region, we progressively obtain all boundary points by successively increasing the primary QoS ρ and solving problem (20). For $\rho = 0$ where backscatter link is prioritized, we initialize Algorithm 1 and 2 by uniform input distribution and Maximum Ratio Transmission (MRT) towards sum cascaded channel $\sum_k \mathbf{h}_{C,k}^H$, respectively. At the following points, both algorithms are initialized by the final solutions at the previous point.

2) *Convergence*: In Fig. 7, we plot the weighted sum of primary and total backscatter rates at $\rho = 0$ for KKT, PGD and BCD algorithms on the first call. For $K = 8$ and $M = 2$, Algorithm 1 typically takes around 100 fast iterations by (23) to converge to the KKT input distribution. For $Q = 4$, around 10 iterations are required for Algorithm 2 to converge, where the gradient is computed by (29) and the step size is refined by BLS. Overall, the BCD algorithm initially requires at most 5 iterations to converge. At the following points (not presented here), the convergence of all three algorithms are much faster thanks to the progressive initialization. Hence, we conclude the proposed algorithms are able to converge fast.

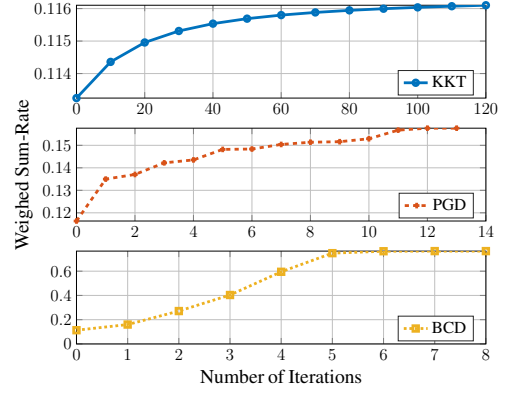


Fig. 7. Typical convergence curves at $\rho = 0$ for $Q = 4$, $K = 8$, $M = 2$, $N = 20$, $\sigma_v^2 = -40\text{dBm}$ and $r = 2\text{m}$.

B. Comparison of Scattering Applications

On top of the setup in Fig. 5, we consider RIScatter and the following benchmark applications:

- *Legacy*: Conventional active transmission without antenna mode scattering, $\alpha = 0$.
- *BBC*: The primary symbol becomes deterministic $s[n] = 1$ and the receive signal at each primary block is

$$y^{\text{BBC}}[n] = \left(\mathbf{h}_D^H + \sum_k \alpha_k \mathbf{h}_{C,k}^H x_k \right) \mathbf{w} + v[n], \quad (36)$$

which follows non-zero mean complex Gaussian distribution $\mathcal{CN}((\mathbf{h}_D^H + \sum_k \alpha_k \mathbf{h}_{C,k}^H x_k) \mathbf{w}, \sigma_v^2)$ under hypothesis \mathcal{H}_{m_K} . The corresponding PDF of accumulated receive energy over N primary blocks is

$$f^{\text{BBC}}(z | \mathcal{H}_{m_K}) = \frac{(z - \mu_{m_K}^{\text{BBC}})^{N-1} \exp(-(z - \mu_{m_K}^{\text{BBC}})/\sigma_v^2)}{\sigma_v^{2N} (N-1)!}, \quad (37)$$

where $\mu_{m_K}^{\text{BBC}} \triangleq N |(\mathbf{h}_D^H + \sum_k \alpha_k \mathbf{h}_{C,k}^H x_k) \mathbf{w}|^2$. The ML decision threshold is derived as, $\forall l \in \mathcal{L} \setminus \{L\}$,

$$t_l^{\text{BBC}} = \frac{\mu_{l-1}^{\text{BBC}} \exp((\mu_{l-1}^{\text{BBC}} - \mu_l^{\text{BBC}})/\sigma_v^2 (N-1)) - \mu_l^{\text{BBC}}}{\exp((\mu_{l-1}^{\text{BBC}} - \mu_l^{\text{BBC}})/\sigma_v^2 (N-1)) - 1}. \quad (38)$$

- *AmBC*: The user decodes both links independently and semi-coherently by treating the other as interference. Hence, the primary achievable rate is approximately⁷

$$I_P^{\text{AmBC}}(s; y) \approx \log \left(1 + \frac{|\mathbf{h}_D^H \mathbf{w}|^2}{\sum_k |\alpha_k \mathbf{h}_{C,k}^H \mathbf{w}|^2 + \sigma_v^2} \right), \quad (39)$$

while the total backscatter rate follows (13) with uniform input distribution.

- *SR*: For a sufficiently large N , the average primary rate under semi-coherent detection asymptotically approaches (16) with uniform input distribution [12]. When $s[n]$ is successfully decoded and the direct interference $\mathbf{h}_D^H \mathbf{w} s[n]$ is perfectly cancelled, the intermediate signal is

$$\hat{y}^{\text{SR}}[n] = \sum_k \alpha_k \mathbf{h}_{C,k}^H x_k \mathbf{w} s[n] + v[n], \quad (40)$$

⁷To provide a preliminary benchmark, we consider the (correlated) scattered signal from finite-input backscatter sources as independent interference from Gaussian sources during primary decoding.

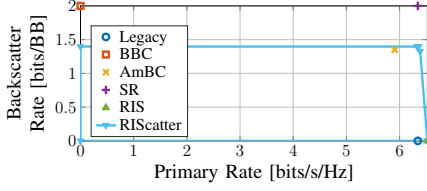


Fig. 8. Typical achievable rate region/points of scattering applications for $Q=1$, $K=1$, $M=4$, $N=1000$, $\sigma_v^2=-40\text{dBm}$ and $r=2\text{m}$.

which only involves noise uncertainty under hypothesis \mathcal{H}_{m_K} . During backscatter detection, the primary symbols $s[1], \dots, s[n]$ can be viewed as a spreading code, and the receiver employs MRC over N primary blocks. The total achievable for nodes with equiprobable inputs is [67]

$$I_B(x_K; \hat{y}_{SR}) = K \log M - \frac{\epsilon}{M^K}, \quad (41)$$

where $\epsilon \triangleq \sum_{m_K} \mathbb{E}_{\hat{v}} \log \sum_{m'_K} \exp(-|x_{m_K} - x_{m'_K} + \hat{v}|^2 / 2\sigma^2)$ and $\hat{v} \sim \mathcal{CN}(0, \sigma_v^2/N)$.

- *RIS*: Since the backscatter symbol tuple x_K is deterministic, the total backscatter rate is zero and the primary achievable rate becomes a special case of (16)

$$I_P^{RIS}(s; y | x_K) = I_P(s; y | x_{m_K}^*) = \log \left(1 + \frac{|h_E^H(x_{m_K}^*) w|^2}{\sigma_v^2} \right), \quad (42)$$

where $m_K^* = \arg\max_{m_K} I_P(s; y | x_{m_K})$.

Fig. 8 compares the typical achievable rate region/points of RIScatter and those applications. *First*, we observe both BBC and SR almost ensure noise-free backscatter transmission when N is sufficiently large. For BBC with coherent energy detection, the conditional PDF of accumulated receive energy (37) is more skewed at a large N , such that the equivalent DMTMAC (9) becomes more reliable. For SR with SIC and MRC, the effective backscatter SNR is increased by N times and the penalty term ϵ becomes insignificant. Such an SR only guarantees the primary benefit with a large N , but decreases the backscatter symbol rate by a factor of N and requires N SIC processes to decode each backscatter symbol (tuple). *Second*, the average primary rate slightly increases/decreases in the presence of a AmBC/RIS node, and the multipath benefit of SR is unobvious. This is because the cascaded channel can be orders of magnitude weaker than the direct channel due to the double fading effect. RIS always ensures constructive superposition of direct and scattered components, while SR only creates a quasi-static rich-scattering environment that stochastically enhances the average primary rate. When N is moderate, the randomly scattered signals should be modelled as primary interference rather than multipath components, and the SR point will move towards the AmBC point. *Third*, RIScatter enables a flexible primary-backscatter tradeoff by smart input distribution design. In terms of maximum primary achievable rate, RIScatter coincides with RIS and outperforms the others by deterministic reflection pattern (no need for backscatter detection). On the other hand, for a large N , the maximum backscatter achievable rate of RIScatter is higher than AmBC but lower than BBC and SR. This is because both RIScatter

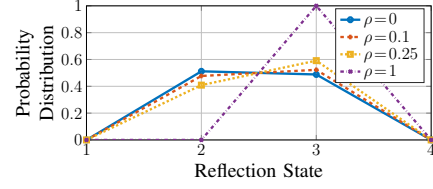


Fig. 9. Typical RIScatter reflection state distribution at different ρ for $Q=1$, $K=1$, $M=4$, $N=20$, $\sigma_v^2=-40\text{dBm}$ and $r=2\text{m}$.

and AmBC employ semi-coherent (instead of coherent) energy detection in the presence of primary uncertainty, and RIScatter with adaptive channel coding can achieve higher backscatter rate than AmBC with equiprobable inputs. Importantly, such a practical RIScatter detection is feasible for arbitrary N , and using a fast-switching node with smaller N can increase the backscatter throughput per unit time while preserving the dynamic passive beamforming gain on the primary link.

C. Input Distribution under Different QoS

The objective of this study is to demonstrate RIScatter nodes can leverage CSI- and QoS-adaptive input distribution design to balance backscatter modulation and passive beamforming. For one RIScatter node with $M=4$, we evaluate the KKT input distribution⁸ at different primary QoS and present the result in Fig. 9. At $\rho=0$ where backscatter performance is prioritized, the optimal input distribution is zero on two states and nearly uniform on the other two. This is because, due to the weak scattered signal, the conditional energy PDF under different hypotheses can be closely spaced as illustrated in Fig. 4. In such cases, the extreme states producing the lowest/highest energy are always assigned with non-zero probability, while the middle ones may not provide enough energy difference and end up unused. At $\rho=1$ where primary performance is prioritized, the optimal input distribution is 1 at the state that maximizes the primary SNR and 0 at the others. That is, the reflection pattern becomes deterministic and the RIScatter node boils down to a discrete RIS element. Increasing ρ from 0 to 1 provides a smooth transition from backscatter modulation to passive beamforming, which demonstrates RIScatter unifies BackCom and RIS from a probabilistic perspective.

D. Rate Region by Different Schemes

1) *Input Distribution*: We compare these input distribution designs for problem (21):

- *Cooperation*: Joint encoding using a K -dimensional probability array $P_K(x_{m_K})$ by Algorithm 1;
- *Exhaustion*: Exhaustive search over the M -dimensional probability simplex with resolution $\Delta p = 10^{-2}$;
- *KKT*: Numerical KKT result evaluation by Algorithm 1;
- *Equiprobable*: Uniform input distribution for all nodes.

Since scatter cooperation is unavailable for dispersed nodes, to support independent encoding, we also consider these input distribution recovery methods over the joint probability array:

⁸Since problem (21) is convex when $K=1$, the KKT solution is also global optimal in this example.

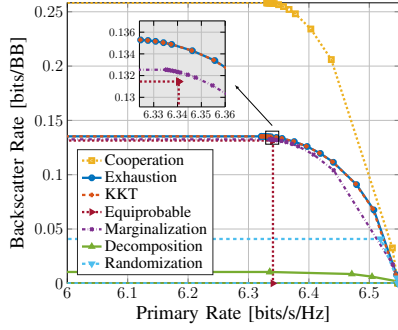
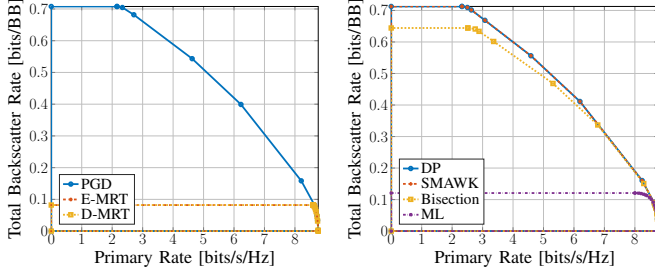
(a) Input Distribution, $Q = 1$ (b) Active Beamforming, $Q = 4$ (c) Decision Threshold, $Q = 4$

Fig. 10. Average primary-total-backscatter rate regions by different input distribution, active beamforming, and decision threshold schemes for $K=2$, $M=4$, $N=20$, $\sigma_v^2 = -40\text{dBm}$ and $r=2\text{m}$.

- *Marginalization*: Marginal probability distributions;
- *Decomposition*: Normalized rank-1 Canonical Polyadic (CP) decomposition tensors by Tensor Toolbox [68];
- *Randomization*: Random search guided by correlation matrix [69].

Fig. 10(a) shows the average achievable rate regions for those designs. *Cooperation* provides the rate region outer bound since joint encoding is generally beneficial for co-located RIScatter nodes. The average rate performance of *Exhaustion* and *KKT* coincide with each other, which demonstrates KKT input distribution can be reasonably good for a moderate K as stated in Remark 3. *Equiprobable* experiences minor backscatter and major primary rate losses without CSI- and QoS-adaptive backscatter encoding. As for the recovery methods, the simple *Marginalization* provides a close result to *KKT*, but *Randomization* and *Decomposition* fail our expectations for most channel realizations. Those observations emphasize the importance of (joint) adaptive RIScatter encoding and demonstrate the advantages of the proposed KKT input distribution design.

2) *Active Beamforming*: We consider three typical active beamforming schemes for problem (24):

- *PGD*: Iterative PGD optimization by Algorithm 2;
- *E-MRT*: MRT towards the ergodic primary equivalent channel $\sum_{m_K} P_K(x_{m_K}) \mathbf{h}_E^H(x_{m_K})$;
- *D-MRT*: MRT towards the direct channel \mathbf{h}_D^H .

Fig. 10(b) presents the average achievable rate regions for those schemes. In the low- ρ regime, the proposed *PGD* beamformer significantly outperforms both MRT schemes in terms of total backscatter rate. This is because backscatter detection relies on the *relative difference* of accumulated receive energy under different hypotheses. Such an energy diversity

is enhanced by *PGD* that effectively exploits backscatter constellation and input distribution knowledge, rather than simply maximizing the direct/ergodic equivalent SNR. As ρ increases, the primary equivalent SNR outweighs the backscatter energy difference in (28), and *PGD* beamformer becomes closer to both MRT schemes. At $\rho=1$, *PGD* and *E-MRT* boil down to MRT towards the deterministic primary equivalent channel as in RIS literature [70]. Besides, the difference between *E-MRT* and *D-MRT* can be insignificant for dispersed RIScatter nodes. Those observations prove the proposed *PGD* active beamforming design can flexibly improve primary equivalent SNR and enhance backscatter energy difference to enlarge the achievable rate region for RIScatter.

3) *Decision Threshold*: We evaluate the following decision threshold strategies for problem (32):

- *DP*: Benchmark DP method for sequential quantizer [64];
- *SMAWK*: *DP* accelerated by the SMAWK algorithm [64];
- *Bisection*: The traverse-then-bisect algorithm [65];
- *ML*: Maximum likelihood detector (33) [66].

Fig. 10(c) reveals the average achievable rate region for those strategies. The distribution-adaptive schemes *DP*, *SMAWK* and *Bisection* ensure higher total backscatter rate than the non-adaptive *ML*. This is because the total backscatter rate (13) is a function of both input distribution and decision regions, and the rate-optimal threshold design heavily depends on input distribution. For example, the backscatter symbol tuples with zero input probability should be assigned with empty decision regions in order to increase the success detection rates of other tuples. It highlights the importance of joint input distribution and decision threshold design in rate maximization problems.

E. Rate Region under Different Configurations

In this study, we choose $Q = 4$, $K = 8$, $M = 2$, $N = 20$, $\sigma_v^2 = -40\text{dBm}$ and $r = 2\text{m}$ as a reference.

1) *Number of Nodes*: Fig. 11(a) reveals how the number of RIScatter nodes K influence the primary-backscatter tradeoff. Interestingly, we observe that increasing K has a larger benefit on the total backscatter rate than primary. This is because each RIScatter node not only affects the primary equivalent SNR but also influences the relative energy difference that other nodes can create. To maximize the total backscatter rate, some nodes closer to the user may need to sacrifice their own rate and use the state that *minimizes* the primary equivalent channel strength, in order to increase the backscatter rate of other nodes. This accounts for the significant primary rate decrease in the low- ρ regime. On the other hand, when the primary link is prioritized, the RIScatter nodes boil down to RIS elements and enjoy a passive array gain of N^2 .

2) *Number of States*: Fig. 11(b) shows the relationship between available reflection states (i.e., QAM order) M and achievable rate regions. We notice increasing the reflection states has a marginal effect on both primary and total backscatter rates. This is because once the scope of reflection coefficient is determined, using denser constellation points may not create enough phase resolution and energy diversity for primary and backscatter links. Due to the maximum amplitude normalization in (2), the average rate region of 8-QAM with rectangular

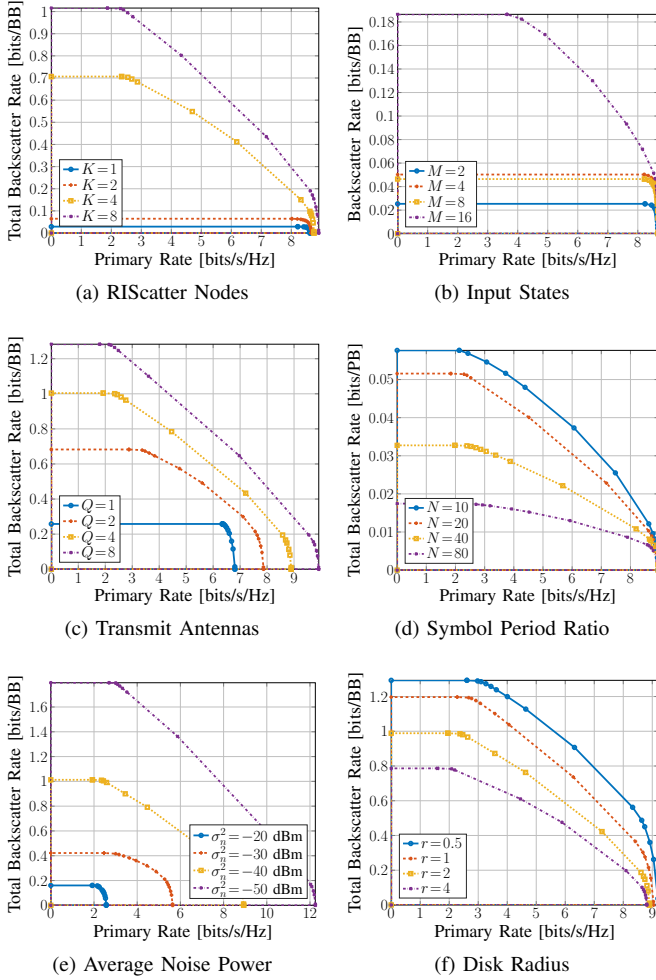


Fig. 11. Average primary-total-backscatter rate regions for different system configurations.

boundary is smaller than that of 4-QAM with square boundary, and the inner constellation points with smaller amplitudes are less frequently used. The results in this and previous paragraphs motivate one to replace the high-resolution metamaterial units of RIS by multiple low-order scatter nodes.

3) *Number of Transmit Antennas*: Fig. 11(c) illustrates the impact of transmit antennas Q on the average performance. Increasing Q enlarges the achievable rate region because PGD provides a flexible tradeoff between primary equivalent SNR and backscatter energy difference. It emphasizes the importance of multi-antenna RISscatter systems and demonstrate the effectiveness of the proposed PGD design.

4) *Symbol Period Ratio*: Fig. 11(d) presents how symbol period ratio N affects the achievable rate region. As mentioned above, the conventional SR scheme with a large N is generally inefficient while RISscatter with a small N can effectively boost the backscatter throughput per unit time. However, it N requires frequent state change that consumes more power at the passive nodes and involves more detection and re-encoding operations at the user. As $N \rightarrow \infty$, RISscatter nodes boil down to RIS elements with fixed reflection pattern during whole channel block and the total backscatter rate approaches 0. Therefore, we conclude N should be properly designed in a practical

RISscatter system based on the data rate requirements, physical constraints at the nodes, and signal processing capability at the user.

5) *Average Noise Power*: Fig. 11(e) depicts the impact of average noise power σ_v^2 on average rate regions. It shows the proposed low-complexity semi-coherent backscatter energy detection is suitable for a wide range of noise levels. When σ_v^2 relatively high, we can choose a longer backscatter symbol period (i.e., larger N) to maintain the backscatter SNR for better detection performance.

6) *Coverage Disk Radius*: Fig. 11(f) shows the relationship between disk radius r and achievable rate region. We observe both primary and backscatter performance are enhanced when nodes are dropped closer to the user. This is because the double fading effect for finite-size scatterers is less severe for near-far setups. In a multi-user RISscatter system with dispersed nodes, each node can be decoded by the nearest user to guarantee uniformly good performance for both links.

VI. CONCLUSION

This paper introduced RISscatter as a low-power scatter protocol that unifies backscatter modulation and dynamic passive beamforming by smart input distribution and practical receiver design. Starting from scattering principles, we showed how RISscatter nodes include information node of BackCom and reflect element of RIS as special cases, how they can be built over existing passive scatter devices, and how they simultaneously encode self information and assist legacy transmission. We also propose a low-complexity RISscatter receiver that preserves the benefits of backscatter modulation and passive beamforming. The achievable primary-total-backscatter rate region is then studied for a single-user multi-node RISscatter system, where the input distribution, active beamforming, and decision thresholds are iteratively updated. Numerical results not only demonstrated the effectiveness of the proposed algorithms, but also emphasized the importance of adaptive input distribution and cooperative decoding on both primary and backscatter subsystems.

One possible direction is to consider backscatter detection over the received signal domain rather than energy domain. Learning-based classification approaches can be promising in such cases. Another interesting question is how to design RISscatter node and receiver in a multi-user system. If one node can be decoded by multiple users, its input distribution may be further adjusted to mimic the multi-beam gain of dynamic passive beamforming [71].

APPENDIX

A. Proof of Proposition 1

Denote the Lagrange multipliers associated with (20b) and (20c) as $\{\nu_k\}_{k \in \mathcal{K}}$ and $\{\lambda_{k,m_k}\}_{k \in \mathcal{K}, m_k \in \mathcal{M}}$, respectively. The Lagrangian function of problem (21) is

$$-I(x_{\mathcal{K}}) + \sum_k \nu_k \left(\sum_{m_k} P_k(x_{m_k}) - 1 \right) - \sum_k \sum_{m_k} \lambda_{k,m_k} P_k(x_{m_k}) \quad (43)$$

and the KKT conditions are, $\forall k, m_k$,

$$-\nabla_{P_k^*(x_{m_k})} I^*(x_{\mathcal{K}}) + \nu_k^* - \lambda_{k,m_k}^* = 0, \quad (44a)$$

$$\lambda_{k,m_k}^* = 0, \quad P_k^*(x_{m_k}) > 0, \quad (44b)$$

$$\lambda_{k,m_k}^* \geq 0, \quad P_k^*(x_{m_k}) = 0, \quad (44c)$$

where directional derivative is explicitly written as

$$\nabla_{P_k^*(x_{m_k})} I^*(x_{\mathcal{K}}) = I_k^*(x_{m_k}) - (1-\rho). \quad (45)$$

Combining (44) and (45), we have

$$I_k^*(x_{m_k}) = \nu_k^* + (1-\rho), \quad P_k^*(x_{m_k}) > 0, \quad (46a)$$

$$I_k^*(x_{m_k}) \leq \nu_k^* + (1-\rho), \quad P_k^*(x_{m_k}) = 0, \quad (46b)$$

such that

$$\sum_{m_k} P_k^*(x_{m_k}) I_k^*(x_{m_k}) = \nu_k^* + (1-\rho). \quad (47)$$

On the other hand, by definition (18) we have

$$\sum_{m_k} P_k^*(x_{m_k}) I_k^*(x_{m_k}) = I^*(x_{\mathcal{K}}), \quad (48)$$

where the right-hand side is irrelevant to k . (46), (47), and (48) together complete the proof.

B. Proof of Proposition 2

We first prove sequence (23) is non-decreasing in weighted sum mutual information. Let $P_{\mathcal{K}}(x_{m_{\mathcal{K}}}) = \prod_{q \in \mathcal{K}} P_q(x_{m_q})$ and $P'_{\mathcal{K}}(x_{m_{\mathcal{K}}}) = \prod_{q \in \mathcal{K} \setminus \{k\}} P'_q(x_{m_q})$ be two probability distributions with potentially different marginal for tag k at state m_k , and define an intermediate function $J(P_{\mathcal{K}}(x_{m_{\mathcal{K}}}), P'_{\mathcal{K}}(x_{m_{\mathcal{K}}}))$ as (49) at the end of page 13. It is straightforward to verify $J(P_{\mathcal{K}}(x_{m_{\mathcal{K}}}), P_{\mathcal{K}}(x_{m_{\mathcal{K}}})) = I(x_{\mathcal{K}})$ and $J(P_{\mathcal{K}}(x_{m_{\mathcal{K}}}), P'_{\mathcal{K}}(x_{m_{\mathcal{K}}}))$ is a concave function for a fixed $P'_{\mathcal{K}}(x_{m_{\mathcal{K}}})$. Setting $\nabla_{P_k^*(x_{m_k})} J(P_{\mathcal{K}}(x_{m_{\mathcal{K}}}), P'_{\mathcal{K}}(x_{m_{\mathcal{K}}})) = 0$, we have

$$S'_k(x_{m_k}) - S'_k(x_{i_k}) + (1-\rho) \log \frac{P_k(x_{i_k})}{P_k^*(x_{m_k})} = 0, \quad (50)$$

where $i_k \neq m_k$ is the reference state and

$$\begin{aligned} S'_k(x_{m_k}) &\triangleq I'_k(x_{m_k}) + (1-\rho) \sum_{m_{\mathcal{K}} \setminus \{k\}} P_{\mathcal{K} \setminus \{k\}}(x_{m_{\mathcal{K}} \setminus \{k\}}) \\ &\times \sum_{m'_k} P(\hat{x}_{m'_k} | x_{m_{\mathcal{K}}}) \log P'_{\mathcal{K}}(x_{m_{\mathcal{K}}}). \end{aligned} \quad (51)$$

Evidently, $\forall m_k \neq i_k$, (50) boils down to

$$P_k^*(x_{m_k}) = \frac{P'_k(x_{m_k}) \exp\left(\frac{\rho}{1-\rho} I'_k(x_{m_k})\right)}{\sum_{m'_k} P'_k(x_{m'_k}) \exp\left(\frac{\rho}{1-\rho} I'_k(x_{m'_k})\right)}. \quad (52)$$

Since $P_k(x_{i_k}) = 1 - \sum_{m_k \neq i_k} P_k^*(x_{m_k})$ has exactly the same form as (52), the choice of reference state i_k does not matter and (52) is indeed optimal $\forall m_k \in \mathcal{M}$. That is, for a fixed $P'_{\mathcal{K}}(x_{m_{\mathcal{K}}})$, choosing $P_k(x_{m_k})$ by (52) ensures

$$J(P_{\mathcal{K}}(x_{m_{\mathcal{K}}}), P'_{\mathcal{K}}(x_{m_{\mathcal{K}}})) \geq I^*(x_{\mathcal{K}}). \quad (53)$$

On the other hand, we also have

$$\Delta \triangleq I(x_{\mathcal{K}}) - J(P_{\mathcal{K}}(x_{m_{\mathcal{K}}}), P'_{\mathcal{K}}(x_{m_{\mathcal{K}}})) \quad (54a)$$

$$\begin{aligned} &= (1-\rho) \sum_{m_k} \frac{P'_k(x_{m_k}) f'_k(x_{m_k})}{\sum_{m'_k} P'_k(x_{m'_k}) f'_k(x_{m'_k})} \sum_{m''_k} P(\hat{x}_{m''_k} | x_{m_k}) \\ &\times \log \frac{\sum_{m'_k} P'_k(x_{m'_k}) P(\hat{x}_{m''_k} | x_{m'_k}) f'_k(x_{m'_k})}{\sum_{m'_k} P'_k(x_{m'_k}) P(\hat{x}_{m''_k} | x_{m'_k}) f'_k(x_{m'_k})} \end{aligned} \quad (54b)$$

$$\begin{aligned} &\geq (1-\rho) \sum_{m_k} \frac{P'_k(x_{m_k}) f'_k(x_{m_k})}{\sum_{m'_k} P'_k(x_{m'_k}) f'_k(x_{m'_k})} \sum_{m''_k} P(\hat{x}_{m''_k} | x_{m_k}) \\ &\times \left(1 - \frac{\sum_{m'_k} P'_k(x_{m'_k}) P(\hat{x}_{m''_k} | x_{m'_k}) f'_k(x_{m'_k})}{\sum_{m'_k} P'_k(x_{m'_k}) P(\hat{x}_{m''_k} | x_{m'_k}) f'_k(x_{m'_k})} \right) \end{aligned} \quad (54c)$$

$$= 0, \quad (54d)$$

where $f'_k(x_{m_k}) \triangleq \exp\left(\frac{\rho}{1-\rho} I'_k(x_{m_k})\right)$ and the equality holds if and only if (52) converges. (53) and (54) together imply $I(x_{\mathcal{K}}) \geq I^*(x_{\mathcal{K}})$. Since mutual information is bounded above, we conclude the sequence (23) is non-decreasing and convergent in mutual information.

Next, we prove any converging point of sequence (23), denoted as $P_k^*(x_{m_k})$, fulfills KKT conditions (22). To see this, let

$$D_k^{(r)}(x_{m_k}) \triangleq \frac{P_k^{(r+1)}(x_{m_k})}{P_k^{(r)}(x_{m_k})} = \frac{f_k^{(r)}(x_{m_k})}{\sum_{m'_k} P_k^{(r)}(x_{m'_k}) f_k^{(r)}(x_{m'_k})}. \quad (55)$$

As sequence (23) is convergent, any state with $P_k^*(x_{m_k}) > 0$ need to satisfy $D_k^*(x_{m_k}) \triangleq \lim_{r \rightarrow \infty} D_k^{(r)}(x_{m_k}) = 1$, namely

$$I_k^*(x_{m_k}) = \frac{1-\rho}{\rho} \log \sum_{m'_k} P_k^*(x_{m'_k}) f_k^*(x_{m'_k}), \quad (56)$$

which is reminiscent of (46a) and (22a). That is, given $P_k^{(0)}(x_{m_k}) > 0$, any converging point with $P_k^*(x_{m_k}) > 0$ must satisfy (22a). On the other hand, we assume $P_k^*(x_{m_k})$ does not satisfy (22b), such that for any state with $P_k^*(x_{m_k}) = 0$,

$$I_k^*(x_{m_k}) > I^*(x_{\mathcal{K}}) = \sum_{m'_k} P_k^*(x_{m'_k}) I_k^*(x_{m'_k}), \quad (57)$$

where the equality inherits from (19). Since the exponential function is monotonically increasing, we have $f_k^*(x_{m_k}) > \sum_{m'_k} P_k^*(x_{m'_k}) f_k^*(x_{m'_k})$ and $D_k^*(x_{m_k}) > 1$. Considering $P_k^{(0)}(x_{m_k}) > 0$ and $P_k^*(x_{m_k}) = 0$, it contradicts with

$$P_k^{(r)}(x_{m_k}) = P_k^{(0)}(x_{m_k}) \prod_{n=1}^r D_k^{(n)}(x_{m_k}). \quad (58)$$

That is, given $P_k^{(0)}(x_{m_k}) > 0$, any converging point with $P_k^*(x_{m_k}) = 0$ must satisfy (22b). The proof is thus completed.

$$J(P_{\mathcal{K}}(x_{m_{\mathcal{K}}}), P'_{\mathcal{K}}(x_{m_{\mathcal{K}}})) \triangleq \sum_{m_{\mathcal{K}}} P_{\mathcal{K}}(x_{m_{\mathcal{K}}}) \left(\rho \log \left(1 + \frac{|\mathbf{h}_E^H(x_{m_{\mathcal{K}}}) \mathbf{w}|^2}{\sigma_v^2} \right) + (1-\rho) \sum_{m'_k} P(\hat{x}_{m'_k} | x_{m_{\mathcal{K}}}) \log \frac{P(\hat{x}_{m'_k} | x_{m_{\mathcal{K}}}) P'_{\mathcal{K}}(x_{m_{\mathcal{K}}})}{P'_{\mathcal{K}}(\hat{x}_{m'_k}) P_{\mathcal{K}}(x_{m_{\mathcal{K}}})} \right). \quad (49)$$

REFERENCES

- [1] C. Boyer and S. Roy, "Backscatter communication and rfid: Coding, energy, and mimo analysis," *IEEE Transactions on Communications*, vol. 62, pp. 770–785, 3 2014. [Online]. Available: <http://ieeexplore.ieee.org/document/6685977/>
- [2] D. Dobkin, *The RF in RFID: Passive UHF RFID in Practice*. Newnes, 11 2012. [Online]. Available: <https://www.elsevier.com/books/the-rf-in-rfid/dobkin/978-0-12-394583-9>
- [3] J. Landt, "The history of rfid," *IEEE Potentials*, vol. 24, pp. 8–11, 10 2005.
- [4] G. Vannucci, A. Bletsas, and D. Leigh, "A software-defined radio system for backscatter sensor networks," *IEEE Transactions on Wireless Communications*, vol. 7, pp. 2170–2179, 6 2008. [Online]. Available: <http://ieeexplore.ieee.org/document/4543069/>
- [5] S. D. Assimonis, S. N. Daskalakis, and A. Bletsas, "Sensitive and efficient rf harvesting supply for batteryless backscatter sensor networks," *IEEE Transactions on Microwave Theory and Techniques*, vol. 64, pp. 1327–1338, 4 2016.
- [6] V. Liu, A. Parks, V. Talla, S. Gollakota, D. Wetherall, and J. R. Smith, "Ambient backscatter: Wireless communication out of thin air," *ACM SIGCOMM Computer Communication Review*, vol. 43, pp. 39–50, 9 2013. [Online]. Available: <https://dl.acm.org/doi/10.1145/2534169.2486015>
- [7] G. Yang, Q. Zhang, and Y.-C. Liang, "Cooperative ambient backscatter communications for green internet-of-things," *IEEE Internet of Things Journal*, vol. 5, pp. 1116–1130, 4 2018. [Online]. Available: <https://ieeexplore.ieee.org/document/8274950/>
- [8] Y.-C. Liang, Q. Zhang, E. G. Larsson, and G. Y. Li, "Symbiotic radio: Cognitive backscattering communications for future wireless networks," *IEEE Transactions on Cognitive Communications and Networking*, vol. 6, pp. 1242–1255, 12 2020. [Online]. Available: <https://ieeexplore.ieee.org/document/9193946/>
- [9] Q. Wu, S. Zhang, B. Zheng, C. You, and R. Zhang, "Intelligent reflecting surface-aided wireless communications: A tutorial," *IEEE Transactions on Communications*, vol. 69, pp. 3313–3351, 5 2021. [Online]. Available: <https://ieeexplore.ieee.org/document/9326394/>
- [10] H. Guo, Y.-C. Liang, R. Long, and Q. Zhang, "Cooperative ambient backscatter system: A symbiotic radio paradigm for passive iot," *IEEE Wireless Communications Letters*, vol. 8, pp. 1191–1194, 8 2019. [Online]. Available: <https://ieeexplore.ieee.org/document/8692391/>
- [11] H. Ding, D. B. da Costa, and J. Ge, "Outage analysis for cooperative ambient backscatter systems," *IEEE Wireless Communications Letters*, vol. 9, pp. 601–605, 5 2020. [Online]. Available: <https://ieeexplore.ieee.org/document/8941106/>
- [12] R. Long, Y.-C. Liang, H. Guo, G. Yang, and R. Zhang, "Symbiotic radio: A new communication paradigm for passive internet of things," *IEEE Internet of Things Journal*, vol. 7, pp. 1350–1363, 2 2020. [Online]. Available: <https://ieeexplore.ieee.org/document/8907447/>
- [13] S. Zhou, W. Xu, K. Wang, C. Pan, M.-S. Alouini, and A. Nallanathan, "Ergodic rate analysis of cooperative ambient backscatter communication," *IEEE Wireless Communications Letters*, vol. 8, pp. 1679–1682, 12 2019. [Online]. Available: <https://ieeexplore.ieee.org/document/8807353/>
- [14] T. Wu, M. Jiang, Q. Zhang, Q. Li, and J. Qin, "Beamforming design in multiple-input-multiple-output symbiotic radio backscatter systems," *IEEE Communications Letters*, vol. 25, pp. 1949–1953, 6 2021. [Online]. Available: <https://ieeexplore.ieee.org/document/9358202/>
- [15] J. Xu, Z. Dai, and Y. Zeng, "Enabling full mutualism for symbiotic radio with massive backscatter devices," *arXiv:2106.05789*, 6 2021. [Online]. Available: <http://arxiv.org/abs/2106.05789>
- [16] Z. Yang and Y. Zhang, "Optimal swipt in ris-aided mimo networks," *IEEE Access*, vol. 9, pp. 112 552–112 560, 2021. [Online]. Available: <https://ieeexplore.ieee.org/document/9494365/>
- [17] S. Han, Y.-C. Liang, and G. Sun, "The design and optimization of random code assisted multi-bd symbiotic radio system," *IEEE Transactions on Wireless Communications*, vol. 20, pp. 5159–5170, 8 2021. [Online]. Available: <https://ieeexplore.ieee.org/document/9382925/>
- [18] Q. Zhang, Y.-C. Liang, H.-C. Yang, and H. V. Poor, "Mutualistic mechanism in symbiotic radios: When can the primary and secondary transmissions be mutually beneficial?" *IEEE Transactions on Wireless Communications*, vol. 1276, pp. 1–1, 2022. [Online]. Available: <https://ieeexplore.ieee.org/document/9751388/>
- [19] R. Torres, R. Correia, N. Carvalho, S. N. Daskalakis, G. Goussetis, Y. Ding, A. Georgiadis, A. Eid, J. Hester, and M. M. Tentzeris, "Backscatter communications," *IEEE Journal of Microwaves*, vol. 1, pp. 864–878, 10 2021. [Online]. Available: <https://ieeexplore.ieee.org/document/9551877/>
- [20] G. Vougioukas and A. Bletsas, "Switching frequency techniques for universal ambient backscatter networking," *IEEE Journal on Selected Areas in Communications*, vol. 37, pp. 464–477, 2 2019. [Online]. Available: <https://ieeexplore.ieee.org/document/8474355/>
- [21] Q. Wu and R. Zhang, "Intelligent reflecting surface enhanced wireless network: Joint active and passive beamforming design," vol. 18. IEEE, 12 2018, pp. 1–6. [Online]. Available: <https://ieeexplore.ieee.org/document/8647620/>
- [22] S. Zhang and R. Zhang, "Capacity characterization for intelligent reflecting surface aided mimo communication," *IEEE Journal on Selected Areas in Communications*, vol. 38, pp. 1823–1838, 8 2020. [Online]. Available: <https://ieeexplore.ieee.org/document/9110912/>
- [23] S. Lin, B. Zheng, F. Chen, and R. Zhang, "Intelligent reflecting surface-aided spectrum sensing for cognitive radio," *IEEE Wireless Communications Letters*, vol. 11, pp. 928–932, 5 2022.
- [24] Y. Liu, Y. Zhang, X. Zhao, S. Geng, P. Qin, and Z. Zhou, "Dynamic-controlled ris assisted multi-user miso downlink system: Joint beamforming design," *IEEE Transactions on Green Communications and Networking*, vol. 6, pp. 1069–1081, 6 2022.
- [25] Z. Feng, B. Clerckx, and Y. Zhao, "Waveform and beamforming design for intelligent reflecting surface aided wireless power transfer: Single-user and multi-user solutions," *IEEE Transactions on Wireless Communications*, 2022.
- [26] Y. Zhao, B. Clerckx, and Z. Feng, "Irs-aided swipt: Joint waveform, active and passive beamforming design under nonlinear harvester model," *IEEE Transactions on Communications*, vol. 70, pp. 1345–1359, 2022.
- [27] Y. Yang, S. Zhang, and R. Zhang, "Irs-enhanced ofdma: Joint resource allocation and passive beamforming optimization," *IEEE Wireless Communications Letters*, vol. 9, pp. 760–764, 6 2020. [Online]. Available: <https://ieeexplore.ieee.org/document/9400457/>
- [28] Q. Wu, X. Zhou, and R. Schober, "Irs-assisted wireless powered noma: Do we really need different phase shifts in dl and ul?" *IEEE Wireless Communications Letters*, vol. 10, pp. 1493–1497, 7 2021. [Online]. Available: <https://ieeexplore.ieee.org/document/9400380/>
- [29] Q. Wu, X. Zhou, W. Chen, J. Li, and X. Zhang, "Irs-aided wpcns: A new optimization framework for dynamic irs beamforming," *IEEE Transactions on Wireless Communications*, pp. 1–1, 12 2021.
- [30] M. Hua and Q. Wu, "Joint dynamic passive beamforming and resource allocation for irs-aided full-duplex wpcn," *IEEE Transactions on Wireless Communications*, pp. 1–1, 12 2021.
- [31] W. Tang, J. Y. Dai, M. Chen, X. Li, Q. Cheng, S. Jin, K. Wong, and T. J. Cui, "Programmable metasurface-based rf chain-free 8psk wireless transmitter," *Electronics Letters*, vol. 55, pp. 417–420, 4 2019. [Online]. Available: <https://onlinelibrary.wiley.com/doi/10.1049/el.2019.0400>
- [32] J. Y. Dai, W. Tang, L. X. Yang, X. Li, M. Z. Chen, J. C. Ke, Q. Cheng, S. Jin, and T. J. Cui, "Realization of multi-modulation schemes for wireless communication by time-domain digital coding metasurface," *IEEE Transactions on Antennas and Propagation*, vol. 68, pp. 1618–1627, 3 2020. [Online]. Available: <https://ieeexplore.ieee.org/document/8901437/>
- [33] R. Karasik, O. Simeone, M. D. Renzo, and S. S. Shitz, "Beyond max-snr: Joint encoding for reconfigurable intelligent surfaces," vol. 2020-June. IEEE, 6 2020, pp. 2965–2970. [Online]. Available: <https://ieeexplore.ieee.org/document/9174060/>
- [34] R. Liu, H. Li, M. Li, and Q. Liu, "Symbol-level precoding design for intelligent reflecting surface assisted multi-user mimo systems," IEEE, 10 2019, pp. 1–6. [Online]. Available: <https://ieeexplore.ieee.org/document/8928065/>
- [35] A. Bereyhi, V. Jamali, R. R. Muller, A. M. Tulino, G. Fischer, and R. Schober, "A single-rf architecture for multiuser massive mimo via reflecting surfaces," IEEE, 5 2020, pp. 8688–8692. [Online]. Available: <https://ieeexplore.ieee.org/document/9052989/>
- [36] X. Xu, Y.-C. Liang, G. Yang, and L. Zhao, "Reconfigurable intelligent surface empowered symbiotic radio over broadcasting signals," vol. 2020-Janua. IEEE, 12 2020, pp. 1–6. [Online]. Available: <https://ieeexplore.ieee.org/document/9348236/>
- [37] Q. Zhang, Y.-C. Liang, and H. V. Poor, "Reconfigurable intelligent surface assisted mimo symbiotic radio networks," *IEEE Transactions on Communications*, vol. 69, pp. 4832–4846, 7 2021. [Online]. Available: <https://ieeexplore.ieee.org/document/9391685/>
- [38] J. Hu, Y. C. Liang, and Y. Pei, "Reconfigurable intelligent surface enhanced multi-user miso symbiotic radio system," *IEEE Transactions on Communications*, vol. 69, pp. 2359–2371, 4 2021.
- [39] M. Hua, Q. Wu, L. Yang, R. Schober, and H. V. Poor, "A novel wireless communication paradigm for intelligent reflecting surface based symbiotic radio systems," *IEEE Transactions on Signal Processing*, vol. 70, pp. 550–565, 4 2022. [Online]. Available: <http://arxiv.org/abs/2104.09161https://ieeexplore.ieee.org/document/9652042/>

- [40] E. Basar, "Reconfigurable intelligent surface-based index modulation: A new beyond mimo paradigm for 6g," *IEEE Transactions on Communications*, vol. 68, pp. 3187–3196, 5 2020. [Online]. Available: <https://ieeexplore.ieee.org/document/8981888/>
- [41] T. Ma, Y. Xiao, X. Lei, P. Yang, X. Lei, and O. A. Dobre, "Large intelligent surface assisted wireless communications with spatial modulation and antenna selection," *IEEE Journal on Selected Areas in Communications*, vol. 38, pp. 2562–2574, 11 2020. [Online]. Available: <https://ieeexplore.ieee.org/document/9133588/>
- [42] J. Yuan, M. Wen, Q. Li, E. Basar, G. C. Alexandropoulos, and G. Chen, "Receive quadrature reflecting modulation for ris-empowered wireless communications," *IEEE Transactions on Vehicular Technology*, vol. 70, pp. 5121–5125, 5 2021. [Online]. Available: <https://ieeexplore.ieee.org/document/9405433/>
- [43] S. Hu, C. Liu, Z. Wei, Y. Cai, D. W. K. Ng, and J. Yuan, "Beamforming design for intelligent reflecting surface-enhanced symbiotic radio systems," *arxiv:2110.10316*, 10 2021. [Online]. Available: <http://arxiv.org/abs/2110.10316>
- [44] Y. C. Liang, Q. Zhang, J. Wang, R. Long, H. Zhou, and G. Yang, "Backscatter communication assisted by reconfigurable intelligent surfaces," *Proceedings of the IEEE*, 2022.
- [45] Q. Wu and R. Zhang, "Towards smart and reconfigurable environment: Intelligent reflecting surface aided wireless network," *IEEE Communications Magazine*, vol. 58, pp. 106–112, 1 2020. [Online]. Available: <https://ieeexplore.ieee.org/document/8910627/>
- [46] R. Hansen, "Relationships between antennas as scatterers and as radiators," *Proceedings of the IEEE*, vol. 77, pp. 659–662, 5 1989. [Online]. Available: <http://ieeexplore.ieee.org/document/32056/>
- [47] S. J. Thomas, E. Wheeler, J. Teizer, and M. S. Reynolds, "Quadrature amplitude modulated backscatter in passive and semipassive uhf rfid systems," *IEEE Transactions on Microwave Theory and Techniques*, vol. 60, pp. 1175–1182, 4 2012. [Online]. Available: <http://ieeexplore.ieee.org/document/6153042/>
- [48] J. Kim and B. Clerckx, "Wireless information and power transfer for iot: Pulse position modulation, integrated receiver, and experimental validation," *IEEE Internet of Things Journal*, vol. 9, pp. 12 378–12 394, 7 2022. [Online]. Available: <https://ieeexplore.ieee.org/document/9651541/>
- [49] X. He, W. Jiang, M. Cheng, X. Zhou, P. Yang, and B. Kurkoski, "Guardrider: Reliable wifi backscatter using reed-solomon codes with qos guarantee," *IEEE*, 6 2020, pp. 1–10. [Online]. Available: <https://ieeexplore.ieee.org/document/9213057/>
- [50] Y. Huang, A. Alieldin, and C. Song, "Equivalent circuits and analysis of a generalized antenna system," *IEEE Antennas and Propagation Magazine*, vol. 63, pp. 53–62, 4 2021. [Online]. Available: <https://ieeexplore.ieee.org/document/9392844/>
- [51] D. Bharadia, K. R. Joshi, M. Kotaru, and S. Katti, "Backfi: High throughput wifi backscatter," vol. 45. *ACM*, 8 2015, pp. 283–296. [Online]. Available: <https://dl.acm.org/doi/10.1145/2785956.2787490>
- [52] G. Yang, C. K. Ho, and Y. L. Guan, "Multi-antenna wireless energy transfer for backscatter communication systems," *IEEE Journal on Selected Areas in Communications*, vol. 33, pp. 2974–2987, 12 2015. [Online]. Available: <http://ieeexplore.ieee.org/document/7274644/>
- [53] H. Guo, Q. Zhang, S. Xiao, and Y.-C. Liang, "Exploiting multiple antennas for cognitive ambient backscatter communication," *IEEE Internet of Things Journal*, vol. 6, pp. 765–775, 2 2019. [Online]. Available: <https://ieeexplore.ieee.org/document/8411483/>
- [54] M. Jin, Y. He, C. Jiang, and Y. Liu, "Parallel backscatter: Channel estimation and beyond," *IEEE/ACM Transactions on Networking*, vol. 29, pp. 1128–1140, 6 2021. [Online]. Available: <https://ieeexplore.ieee.org/document/9377568/>
- [55] B. Zheng and R. Zhang, "Intelligent reflecting surface-enhanced ofdm: Channel estimation and reflection optimization," *IEEE Wireless Communications Letters*, vol. 9, pp. 518–522, 4 2020. [Online]. Available: <https://ieeexplore.ieee.org/document/8937491/>
- [56] C. You, B. Zheng, and R. Zhang, "Intelligent reflecting surface with discrete phase shifts: Channel estimation and passive beamforming," *IEEE*, 6 2020, pp. 1–6. [Online]. Available: <https://ieeexplore.ieee.org/document/9149292/>
- [57] J. Qian, F. Gao, G. Wang, S. Jin, and H. Zhu, "Semi-coherent detection and performance analysis for ambient backscatter system," *IEEE Transactions on Communications*, vol. 65, pp. 5266–5279, 12 2017. [Online]. Available: <http://ieeexplore.ieee.org/document/8007328/>
- [58] T. Nguyen, Y.-J. Chu, and T. Nguyen, "On the capacities of discrete memoryless thresholding channels," vol. 2018-June. *IEEE*, 6 2018, pp. 1–5. [Online]. Available: <https://ieeexplore.ieee.org/document/8417506/>
- [59] T. Nguyen and T. Nguyen, "Optimal quantizer structure for maximizing mutual information under constraints," *IEEE Transactions on Communications*, vol. 69, pp. 7406–7413, 11 2021. [Online]. Available: <https://ieeexplore.ieee.org/document/9530430/>
- [60] M. Rezaeian and A. Grant, "Computation of total capacity for discrete memoryless multiple-access channels," *IEEE Transactions on Information Theory*, vol. 50, pp. 2779–2784, 11 2004. [Online]. Available: <http://ieeexplore.ieee.org/document/1347364/>
- [61] J. Buhler and G. Wunder, "A note on capacity computation for the discrete multiple access channel," *IEEE Transactions on Information Theory*, vol. 57, pp. 1906–1910, 4 2011. [Online]. Available: <https://ieeexplore.ieee.org/document/5730559/>
- [62] G. J. O. Jameson, "The incomplete gamma functions," *The Mathematical Gazette*, vol. 100, pp. 298–306, 7 2016. [Online]. Available: https://www.cambridge.org/core/product/identifier/S002555721600067X/type/journal_article
- [63] S. Boyd and L. Vandenberghe, *Convex Optimization*. Cambridge University Press, 3 2004. [Online]. Available: <https://www.cambridge.org/core/product/identifier/9780511804441/type/book>
- [64] X. He, K. Cai, W. Song, and Z. Mei, "Dynamic programming for sequential deterministic quantization of discrete memoryless channels," *IEEE Transactions on Communications*, vol. 69, pp. 3638–3651, 6 2021. [Online]. Available: <https://ieeexplore.ieee.org/document/9366549/>
- [65] T. Nguyen and T. Nguyen, "On thresholding quantizer design for mutual information maximization: Optimal structures and algorithms," vol. 2020-May. *IEEE*, 5 2020, pp. 1–5. [Online]. Available: <https://ieeexplore.ieee.org/document/9128966/>
- [66] J. Qian, A. N. Parks, J. R. Smith, F. Gao, and S. Jin, "Iot communications with m-psk modulated ambient backscatter: Algorithm, analysis, and implementation," *IEEE Internet of Things Journal*, vol. 6, pp. 844–855, 2 2019. [Online]. Available: <https://ieeexplore.ieee.org/document/8423609/>
- [67] J. Wang, N. Li, W. Shi, Y. Ma, X. Liang, and X. Dong, "Capacity of 60 ghz wireless communications based on qam," *Journal of Applied Mathematics*, vol. 2014, pp. 1–5, 2014. [Online]. Available: <http://www.hindawi.com/journals/jam/2014/815617/>
- [68] B. W. Bader and T. G. Kolda, "Tensor toolbox for matlab," 9 2022.
- [69] E. Calvo, D. P. Palomar, J. R. Fonollosa, and J. Vidal, "On the computation of the capacity region of the discrete mac," *IEEE Transactions on Communications*, vol. 58, pp. 3512–3525, 12 2010. [Online]. Available: <http://ieeexplore.ieee.org/document/5590317/>
- [70] Q. Wu and R. Zhang, "Intelligent reflecting surface enhanced wireless network via joint active and passive beamforming," *IEEE Transactions on Wireless Communications*, vol. 18, pp. 5394–5409, 11 2019. [Online]. Available: <https://ieeexplore.ieee.org/document/8811733/>
- [71] C. Qiu, Q. Wu, M. Hua, X. guan, and Y. Wu, "Achieving multi-beam gain in intelligent reflecting surface assisted wireless energy transfer," *arXiv:2205.08893*, 5 2022. [Online]. Available: <http://arxiv.org/abs/2205.08893>